The human factor: development and characterization of a scalable calcium imaging assay using human iPSC-derived neurons

Martin Dietrich Haustein[1], Caroline Deymier[1,#], Simon Schlienger[1,#], Laurane Lexcellent-Bissler[1], Jacques Mawet[1], Eric Gutknecht[1], Laure Thenoz[1], Pijus Brazauskas[1], Bérengère Renault[1], Stéphanie Brun[1], Simone Winistörfer[1], and Thomas Portmann[1,*]

[1]CNS Translational Sciences, Idorsia Pharmaceuticals Ltd, Allschwil, Switzerland

[#]These authors equally contributed to the study

*** Correspondence:**
Thomas Portmann
thomas.portmann@idorsia.com

Keywords: human iPSC, reprogramming, calcium imaging, GABA inhibition, DAPT, oscillation assay, neural network activity.

Abstract

Neuroscience drug discovery is challenged by the brain's structural and cell-type complexity, which is difficult to model in cellular systems compatible with high-throughput screening methods. Calcium oscillation assays, that harness neurons' intrinsic capability to develop functional neural networks in cell culture, are currently the closest cellular models with a relevant functional endpoint to model human neuronal circuitry in a dish. Here we further develop this useful assay towards scalable drug discovery applications. We show the importance of defined neuron-to-astrocyte ratios for optimal cellular distribution and surface adherence in HTS-compatible cell culture vessels and how the cell type ratios determine network firing patterns. We identify DAPT, a molecule previously shown to promote neuronal maturation and synapse formation, as a negative regulator of astrocyte viability. Addition of GABA-ergic inhibitory neurons increases the network spike frequency while reducing network spike amplitudes. We develop a pixel-based analysis for plate reader data to access local field activity in an automated and scalable calcium imaging environment. Using this method, we identify a desynchronization of excitatory neuronal activity by GABA neurons that echoes GABA action in vivo, and dysregulation thereof in pathological conditions.

1 Introduction

Drug discovery efforts to address pathological conditions of the central nervous system (CNS) have historically suffered from a lack of clinically translatable in vitro systems that are useful both for high-throughput screening (HTS) and efficient downstream evaluation of candidate molecules. While the integration of single-cell resolution technologies in neuroscience research has advanced our understanding of pathological mechanisms in the neural circuitry and in specific neuronal and glial cell types, modeling these mechanisms in cell culture systems has remained a challenge. This is due mainly to the complexity of the CNS architecture, with a myriad of different cell types interacting in health and disease, as well as due to the difficulty of generating precise replica cell types of translational relevance in a cell culture dish. The latter is of particular importance as some of the most promising drug targets in the CNS including G-protein coupled receptors are found to be expressed in unique and highly cell type-selective patterns. Hence, replicating (1) the precise CNS

cell type(s) of interest for drug treatment in patients and (2) their endogenous target expression including the surrounding protein signaling interactome is of utmost importance to properly assess the translational potential of candidate compounds early in the CNS drug discovery process.

The discovery of somatic reprogramming and the development of protocols for differentiation of human induced pluripotent stem cells (iPSC) into neurons has helped the field to overcome major limitations imposed by the inaccessibility of live human CNS tissue for research (Takahashi et al., 2007). Importantly, human iPSC offered new opportunities to complement rodent CNS-derived in vitro models and heterologous expression systems with human CNS cell types in drug discovery research. While early iPSC-derived in vitro CNS models were generated by neuronal differentiation protocols taking embryonic brain development as template (Brennand et al., 2011; Paşca et al., 2011; Shcheglovitov et al., 2013), cellular reprogramming by transcription factor over-expression is increasingly adopted for properties that are easier reconciled with scalability in drug discovery assays (Saavedra et al., 2021; Yang et al., 2017; Zhang et al., 2013). These properties include the rapid and relatively homogeneous generation of specific neuron or glia types within days. Scaled production and cryopreservation of reprogrammed CNS cell types further allow for rapid integration into assays without the need of starting from pluripotent stem cells. Essentially, the focus is on generating cell types “close enough” to their in vivo counterparts with regards to target expression and key functional properties. And this, achievable with relatively simple, rapid, and robust cell culture protocols. Transcription factor-based reprogramming allows for comparably efficient generation of highly pure human in vitro CNS-like cell types. Combinations of specific transcriptions factors, further termed herein reprogramming codes, allow for generation of induced neurons, including glutamatergic excitatory neurons (GLUT iN, reprogramming code: Ngn2)(Zhang et al., 2013), GABA-ergic inhibitory neurons (GABA iN: Ascl1 and Dlx2)(Yang et al., 2017), and various glia types that resemble key CNS cell types of the human brain.

A mainstay of CNS drug discovery and development is the calcium oscillation assay, which allows for rapid assessment of key functional properties of neuronal networks and their modulation by therapeutic candidate molecules. In this assay, synchronized firing of an entire neural network results in globally oscillating calcium signals that can be measured on plate readers based on fluorescent signals from calcium-sensitive dyes or genetically encoded calcium indicators. For development of synchronized neural network activity of human GLUT iN, astrocyte-derived factors to support synapse formation and maturation are key. The simplest way of providing these factors is by culturing neurons in astrocyte-conditioned medium (Shan et al., 2024). The alternative is co-culturing neurons with astrocytes in order to allow for astrocytes to provide real-time metabolic support and actively modulate synapse development. Rodent astrocytes from fetal or neonate brain have widely been used for ease of access (Patzke et al., 2015). Primary fetal astrocytes (pA) of human origin in turn allow for development of oscillation assays of completely human cellular origin (Bassil et al., 2021; Saavedra et al., 2021). However, while many versions of calcium oscillation assays using human neurons have been presented, few only did so within a scalable environment. For example, multi-week protocols for human neuron-based calcium oscillation assays often still include use of low-throughput surfaces, such as glass coverslips (Sun & Südhof, 2021). With few exceptions, the precise ratio of neurons and astrocytes for optimal network development, and how it affects oscillation characteristics has not been described in detail, and finally, key cell culture properties including cell attachment and cellular distribution in 2D (versus aggregate formation) and their impact on calcium signals remain underexplored. Also, the importance of GABAergic inhibition, important for control and synchronization of neural network activity in vivo and playing an

important role in therapeutic action of psychiatric and anti-epileptic drugs, merits further exploration in the context of all-human in vitro neural network models.

Here, we set out to test various parameters of a human GLUT iN-based calcium oscillation assay, towards scalable applications including drug screening on fully functional neural networks. We characterized key parameters to allow for implementation in a standard high-throughput environment, including culture on HTS-capable optical cell culture plates, and the impact of neuron-astrocyte ratios on firing properties. We find that neuron-astrocyte ratios dictate not only network firing properties, but also cellular attachment and the tendency of GLUT iN to form clusters or remain evenly distributed over time. We show that brief treatment with DAPT, a gamma secretase inhibitor changes the ratio of neurons and astrocytes by selectively decreasing the viability of astrocytes. And finally, we find that GABA iN-mediated network inhibition changes network firing properties by reducing the synchronization of neuronal firing across the well surface as demonstrated by a novel, pixel-resolution analysis of plate reader data.

2 Materials and methods

2.1 Human iPSC culture and engineering

Human iPSCs were cultured in mTeSR Plus on Geltrex coated cell culture vessels (1:100 in DMEM/F12) at 37°C, 5% CO_2 and >90% humidity. Cells were passaged as aggregates by incubating them for 5 min at 37°C with ReLeSR and seeding them in mTeSR Plus supplemented with 2 µM Thiazovivin for less than 24 h.

For CRISPR-based genome engineering, RNP complexes were prepared in two steps. First, the crRNA and tracrRNA-ATTO 550 were mixed at 5 µM in Neon Resuspension buffer R, heated to 95 °C and slowly cooled down to room temperature. Then the newly formed gRNA was incubated at 4 µM with HiFi Cas9 nuclease V3 at 1.4 µM for 20 min at room temperature. Cells were incubated in mTeSR Plus supplemented with 1x CloneR2 for 1 h, and subsequently detached with Accutase for 8 min at 37°C. The cells were pelleted at 300 g for 5 min and resuspend in Neon Resuspension buffer R at 60’000 cells/µl. 7.5 µl cell suspension was mixed with 5 µl RNP complexes and 2.5 µl donor plasmid (1.5 µg in Neon Resuspension buffer R). 10 µl was aspirated with the Neon pipette and electroporated with a single 30 ms pulse at 1’100 V. Immediately afterwards, the cells were transferred to a Geltrex coated a 6-well plate containing mTeSR Plus supplemented with 1x CloneR2 and 20 µM HDR-Enhancer V1 and incubated at 32°C, 5% CO_2. After 2 days, the medium was replaced with mTeSR Plus supplemented with the appropriate selection antibiotic (Puromycin: 0.3 µg/ml / Blasticidin: 2 µg/ml) and the cells were continuously monitored. Clonal selection was either performed by limiting dilution in 96-well plates or by sparce single cell seeding in 10 cm dishes and manual colony picking.

For Cre recombinase-mediated cassette exchange (RMCE), cells were treated with 1 µg/ml doxycycline for 24 h before electroporation. Single-cell suspension in Neon Resuspension buffer R was prepared as described above and mixed with 1.5 µg donor plasmid, diluted in 7.5 µl Neon Resuspension buffer R. 10 µl of the mix was electroporated with a triple 20 ms pulse at 1’200 V. Immediately afterwards, the cells were transferred to a Geltrex coated 6-well plate containing mTeSR Plus supplemented with 1x CloneR2. After 2 days, the medium was replaced with mTeSR Plus supplemented with 2 µg/ml Blasticidin. Clonal selection was either performed by limiting dilution in 96-well plates or by sparce single cell seeding in 10 cm dishes and manual colony picking. All iPSC lines were checked by karyotyping and the master iPSC and Bi-GCaMP6f-2A-RFP lines were further

checked for microdeletions or microduplications by array comparative genomic hybridization. Pluripotency marker staining was occasionally included to spot-check pluripotency state of the cell.

Donor DNA constructs were generated by gene synthesis (GeneScript, Azenta). Schematic views are shown for donor constructs for homology-directed repair (HDR) (Fig S1A, Fig S4A,C) and RMCE (Fig 3A). For HDR constructs, the selection cassettes were flanked by compatible Lox sites (LoxFas and LoxN, for the puromycin N-acetyltransferase, *pac*, and blasticidin S deaminase, *bsr*, genes respectively). A Cre recombinase coding sequence was coupled to EGFP via a P2A sequence and put under control of a tetracycline responsive Tet-ON promoter. A reverse Tet transactivator (rtTA) coding sequence was put under control of the constitutive CAGGS promoter (Hitoshi et al., 1991). Selection cassettes flanked by compatible Lox sites were removed in the final master iPSC line by brief exposure to doxycycline to enable their reuse for integration of additional DNA modules. The Cre transgene was flanked by incompatible Lox sites (LoxP and Lox2272). Upstream of the Tet-ON promoter in opposite direction, a *bsr* gene without promoter was placed to enable selection for RMCE upon integration of a reprogramming code. RMCE donor constructs contained the reprogramming code ASCL1+DLX2 (coupled by a 2A sequence) under control of a Tet-ON promoter. Furthermore, a CAGGS promoter was placed upstream in the opposite direction to drive *bsr* and enable selection for genomic integration by RMCE. The donor DNA of the RMCE contructs were flanked by incompatible LoxP and Lox2272 sites matching the replacement cassette in the master iPSC. The herein presented design of iPSC lines served the sole purpose of assay feasibility evaluation, and any future use in, for example, drug discovery research may require further optimization.

For PCR genotyping, cells were washed DPBS and incubated with 80-100 µl/cm^2 Lysis solution (Tris-HCl: 10 mM, KCl: 50 mM, $MgCl_2$: 2 mM, Gelatin: 0.1 mg/ml, IGEPAL: 0.45%, Tween-20: 0.45%, Proteinase K: 100 µg/ml) for 3 min. The lysates were collected and incubated at 55 °C for 4 h, followed by Proteinase K deactivation at 95 °C for 10 min. gDNA was then amplified by PCR with Platinum™ Hot Start PCR Master Mix. Reagent item numbers and primer sequences are provided in Table S1.

2.2 Neural reprogramming of human iPSC and neuron-astrocyte co-culture

Human iPSCs were detached with Accutase for 8 min at 37°C, pelleted at 300 g for 5 min, resuspended in mTeSR Plus supplemented with 2 µM Thiazovivin and seeded on Matrigel coated culture vessels at a density of 10’000 cells/cm^2. From d1 to d3 the medium was exchanged to reprogramming medium (DMEM/F12 supplemented with N2, NEAA, 10 ng/ml hBDNF, 10 ng/ml hNT-3, 200 ng/ml mouse laminin, and 2 µg/ml doxycycline) and renewed daily. On d4 the young neurons were detached with Accutase for 6 min at 37°C, pelleted at 300 g for 5 min and either resuspended in Bambanker for cryopreservation or in Neuronal medium (Neurobasal-A supplemented with B27, GlutaMAX, 10 ng/ml hBDNF, 10 ng/ml hNT-3, 200 ng/ml mouse laminin, and 2 µg/ml doxycycline) for co-culture with astrocytes. Reprogramming was monitored by microscopy and samples for viability assays were collected at selected timepoints.

On d2 of reprogramming, human primary astrocytes were seeded on laminin (20 µg/ml in DPBS) coated culture cell culture plates (Perkin Elmer phenoplate) in Astrocyte medium. After 2 days, the medium was switched to Neuronal medium and young neurons (d4) were seeded on top. Half-media changes were performed every 2-3 days. From d7-d10, the neuronal medium was supplemented with 2 µM Ara-C and from d11 onwards with 2.5% FBS. The co-cultures were monitored by microscopy and samples for viability assays were collected at selected timepoints.

2.3 Cell viability assays

LDH assay was performed with the CytoTox 96 non-radioactive assay, according to manufacturer's protocols. Briefly, cell culture conditioned medium was collected and 12.5 µl were transferred in duplicate or in triplicate into a 384 well plate, spun down, and supplemented with 12.5 µl of CytoTox 96 Reagent. After 15-30s mix with a plate shaker, assay plate was incubated 30 minutes at room temperature, light protected. Reaction was stopped by adding 12.5 µl of Stop Solution, mixed 15-30s with a plate shaker, light protected, and absorbance was red immediately (or within one hour) at 490 nm with the SynergyMX, without lid. Cell culture medium served as control. Data processing and analysis was performed according to manufacturer's recommendations.

Incucyte® Caspase-3/7 Green Dye was used according to manufacturer's instructions. Briefly, 5 µM in Dye was diluted in culture medium and phase and fluorescent images were acquired with the Incucyte SX5 every 2h. Masks for the cell confluence and the dye fluorescence were directly generated in the Incucyte software.

2.4 Single-Nucleus RNA Sequencing (snRNA-seq) Library Preparation and Sequencing

To prepare single-nuclei suspensions for snRNA-seq, co-cultures plates were placed on ice for 1 min and medium was removed. 20 µL/well of cold Lysis buffer (1x PBS, Tris-HCl 10 mM, NaCl 10 mM, $MgCl_2$ 3mM, NP40 0.025%, pH7.4) were added and cells were kept on ice for 3 min with 3-5 times gently mix using micropipette. Lysis was stopped by adding 4x lysis buffer volume of cold Nuclei Wash and Resuspension Buffer (NWR Buffer) (1x PBS, 1% BSA, RNase Inhibitor 0.2 U/µl). The nuclei suspensions were collected in a microplate and centrifuged for 10 min at 500 rcf, 4°C using swinging-bucket rotor. Supernatants were removed and nuclei pellets were resuspended in 180 µL of NWR buffer and then centrifuged at 500 rcf for 10 min at 4°C. The washing step was repeated once more and the nuclei were resuspended in 1x PBS containing 0.04% BSA.

3' CellPlex Kit Set A was used for nuclei labeling. Before use, Cell Multiplexing Oligo (CMO) were thawed 30 min at room temperature, then vortexed 5 sec at maximum speed and centrifuged briefly for 5 sec. Supernatants were removed and nuclei were resuspended with 20 µL CMO with 15x gentle pipette mix. Labeling was done for 5 min at room temperature. 9x CMO volume of cold NWR Buffer was added and nuclei were centrifuged at 500 rcf for 10 min at 4°C. Supernatants were completely removed, and nuclei pellets were resuspended in 180 µl of cold NWR Buffer then centrifuged at 500 rcf for 10 min at 4°C. The washing step was repeated two times for a total of 3 washes. Nuclei concentration was quantified using Luna-FX7 automated cell counter and then diluted to 1500 cells/uL for subsequent snRNA-seq experiment.

Single-nucleus RNA-seq libraries were prepared using Chromium Next GEM Single Cell 3′ Reagent Kit v3.1 (10x Genomics) according to the manufacturer's protocol (CG000388). Briefly, single nuclei were captured, barcoded, and reverse-transcribed, followed by cDNA amplification and library construction. Library size distribution was assessed using Fragment Analyzer NGS High Sensitivity Kit (Agilent Technologies), and library concentrations were quantified using KAPA Library Quantification Kit (Roche Diagnostics) according to the manufacturer's instructions. Cell Multiplexing Oligo (CMO) libraries and gene expression libraries were pooled at a 1:4 molar ratio and sequenced on an Illumina NextSeq 2000 platform using a P2 100-cycle kit (Illumina).

Sequencing reads were aligned to the human reference genome (GRCh38; GENCODE v32/Ensembl 98) using the Kallisto bustools (kb-python) pipeline with the -nac parameter to obtain single-cell gene count matrices (Melsted et al., 2021). CMO assignment was performed using Cell Ranger v7.2.0 (10x Genomics).

For cell type annotation and clustering, cell type specific genes were identified by correlation to known cell type-specific marker genes. In addition, cell type-specific genes were confirmed based on the Jensen-Shannon divergence of their expression distribution from the expression distribution of a hypothetical, perfectly specific gene (Lin, 1991). Graphing was done using Python as described under Statistical analysis and graphing.

2.5 Calcium imaging

Calcium imaging was conducted at d28-31 as indicated. All recordings were performed using the FDSS7000EX (Hamamatsu) at 37°C. Co-cultures were gently washed with modified Tyrode solution (25 mM HEPES, 150 mM NaCl, 5 mM KCl, 1 mM $MgCl_2$, 10 mM glucose, 2 mM $CaCl_2$, pH 7.2–7.4, pre-warmed to 37 °C), then incubated with calcium imaging buffer (25 mM HEPES, 150 mM NaCl, 8 mM KCl, 1 mM $MgCl_2$, 10 mM glucose, 4 mM $CaCl_2$, pH to 7.2–7.4, pre-warmed to 37°C). After 20 min equilibration at 37°C, calcium imaging was performed as follows: GCaMP6f fluorescence was recorded for 5 or 10 min at a frame rate of 5 frames/s with binning 2x2 for standard recording and at a frame rate of 8 frames/s binning 1x1 for pixel-resolution. Compounds were prepared in calcium imaging buffer containing 0.1% BSA and were added during acquisition 5 min after recording start. For calcium imaging assays performed with Calcium-dye, co-cultures were incubated for 90 min at 37°C, 5% CO2 with Calcium6 dye (Molecular Devices) dissolved in calcium imaging buffer then fluorescence was recorded as described above.

2.6 Calcium imaging data analysis

For the detection of network spikes, the function find_peaks() from the Scipy package (Virtanen et al., 2020) in Python was used and peak prominences of the calcium signals were extracted for each well. Global detection thresholds for each plate were set based on the background signal from empty wells at the outer edges of each plate. From the total number of network spikes in a given time period the frequency was calculated. For analysis of calcium traces at pixel-resolution, Scipy find_peaks() function was used. A prominence-based detection threshold of 0.4 was applied for local field spike detection, unless otherwise mentioned.

2.7 Immune-cytochemistry

After removal of medium or calcium imaging buffer, the co-cultures were fixed with 4% PFA for 10 min at room temperature (RT), then washed three times with 1xPBS. Blocking and permeabilization were done by 1h incubation at RT with 1x PBS containing 0.3% Triton X-100 and 5% Goat serum. Primary antibodies were diluted in blocking buffer (1% BSA and 0.3% Triton X-100 in PBS) at 4°C for 16-20h then washed 3 times with 1xPBS. Secondary antibodies incubation was done for 1h at RT in blocking buffer containing Hoechst 33342 followed by 4 washes in 1× PBS. Fluorescence acquisition was done using the Yokogawa CQ1 confocal imaging system, 6 slices with 10 µm Z range.

2.8 Nuclei counting

As part of the antibody-staining protocol above the plates were stained with Hoechst. Images were acquired on the Yokogawa CQ1 confocoal imaging system with at least 6 planes with 10 µm Z-range of at least 6 fields of view per well). Stardist (Schmidt et al., 2018; Weigert & Schmidt, 2022) was trained on a dozen of images of neuronal and astrocyte nuclei based on RFP and Sox9 expression, respectively, and dead cell nuclei (excluded).

2.9 Enzyme-linked immunosorbent assay (ELISA) for GABA

GABA levels in the culture medium were measured with the human GABA ELISA kit (ImmusMol) in accordance with the manufacturer's instructions.

2.10 Statistical analysis and graphing

All experiments were replicated multiple times. Representative experiments are shown. Pooling of data across experiments was purposefully avoided in order to display the variability of data across experiments and wells, which needs consideration given the length and complexity of these multi-week cell culture assays. Endpoint measurements were performed between d28 and d31 of co-culture, as mentioned. All comparisons were restricted to within-experiment. Statistical tests were used as indicated and corrected for multiple comparisons (Bonferroni correction). Two-way Anova test was performed using the statsmodels.stats.anova.anova_lm() function. Scipy Statistics TTEST_ind() unpaired T-test was applied for across-well comparisons. Scipy Statistics TTEST_rel() paired T-test was applied for within-well comparisons for drug treatment versus baseline activity.

Graphing was done using python seaborn statistical data visualization modules including heatmap(), clustermap(), lineplot(), stripplot(), boxplot(). Box plots denote 2nd and 3rd quartile (semitransparent box area), with bars extending to 1.5 times the interquartile range of the lower and upper quartile (IQR). Individual datapoints are overlaid as dots. Line plots denote the 95% confidence interval around the mean, either as error bars or semi-transparent area, unless otherwise indicated. Scanpy.tl.tsne() function was used for t-distributed stochastic neighborhood embedding (Maaten & Hinton, 2008; Wolf et al., 2018). Scipy.stats.entropy() was used to calculate the relative entropy of gene expression distributions. Correlation analyses used the pandas.DataFrame.corr() function.

3 Results

3.1 Development of an all-human in vitro calcium oscillation assay.

To investigate key parameters relevant for calcium signals from in vitro human neural networks we opted for a basic setup comprised of cortical-like excitatory neurons and astrocytes, which was adapted from previous reports (Bassil et al., 2021; Sun & Südhof, 2021; Zhang et al., 2013). Neurons were generated by reprogramming of a stable iPSC line (BIONi010-C-13) using inducible overexpression of the human neurogenic transcription factor NGN2, as previously described and characterized including by electrophysiology (Fig 1A schematic)(Schmid et al., 2021; Shih et al., 2021). To enable measurement of calcium signals, we modified these neurogenic iPSC to express a single copy of GCaMP6f genetically encoded calcium indicator (Chen et al., 2013),which was coupled to RFP via a 2A sequence, from the ROSA26 locus (Bertero et al., 2016) and put under the control of a constitutive CAGGS promoter (Fig 1A, Fig S1A)(Hitoshi et al., 1991). This new iPSC line was termed Bi-GCaMP6f-2A-RFP. Human pA were seeded on day in vitro (d) 2 and GLUT iN replated for co-culture with the astrocytes on d4. RFP expression provided a means for monitoring

overall neuronal density and distribution over time of culture in each well. Cell viability was monitored by Lactate dehydrogenase (LDH) activity in samples taken before each media change. Remaining cell proliferation, which was mainly expected to arise from the pA, was terminated by a defined period of Ara-C treatment from d7 to d10. FBS was supplemented from d11 onwards and cells subjected to terminal analyses between d28 to d31, as indicated. By this stage, neurons had developed dense neuritic networks and robustly expressed GCaMP6f, as well as RFP (Fig 1B).

The early phase of NGN2-driven neural reprogramming using the parent neurogenic iPSC line has previously been described (Schmid et al., 2021). In terms of cell morphology and density between d0 and d4, cells behaved comparably in our experimental setup displaying dispersion of iPSC colonies within 1-2 days of doxycycline-induced NGN2 over-expression, and a rapid decline of proliferation as well as appearance of neuronal-like cell morphology by d4 (Fig S1B). We compared the co-culture phase of neurons with astrocytes (d4 onward) in 96-well and 384-well plate formats. Two widely used coating conditions, laminin versus Matrigel were tested. Due to lower viscosity and associated ease-of-handling, Matrigel was replaced by the similar Geltrex matrix when switching to 384-well plate format. Co-culture conditions were tested at different ratios and densities of neurons and astrocytes. Overall, co-cultures behaved similarly on the tested coating conditions for various parameters (Fig S1C,D,G). LDH activity remained overall low, except for a spike upon treatment with Ara-C (d7-d10), which declined after gradual washout with subsequent half-media changes, thus indicating an AraC-induced loss of cells (Fig S1C). Furthermore, average LDH activity across time was more strongly impacted by the number of initially seeded astrocytes at d2 (two-way p_{ANOVA} = 7.37E-17 and 2.54E-09 on Matrigel and Laminin, respectively) than by the number of replated neurons at d4 (p= 9.35E-1 and 5.14E-03) without interaction between the two (p = 0.105 and 0.994 on Matrigel and Laminin, respectively). These results indicate that the major cell type retaining some degree of cell proliferation into week 2 of the assay are the pA and, consistent with this, that neuron viability is comparably less affected by Ara-C treatment.

3.2 The cell type ratio determines cellular distribution and surface adherence.

Over the course of 3-4 weeks of co-culture, the cellular composition (i.e., ratio and seeding densities of GLUT iN and pA) affected cellular distribution and attachment to the well surface, as observed by monitoring of the RFP expression in the GLUT iN (Fig S1D). In the 384-well plate format, astrocyte numbers below 2k per well resulted in redistribution of neural networks to form clusters and further condense into a ring-shaped “super-cluster” that developed over the course of the co-culture phase in an outside-in fashion (Figure 1 C,D)). A similar phenomenon was observed in 96-well plate format at pA densities lower than 10k (Fig S1E). The cellular composition also impacted the ability of cells to adhere to the well surface over the course of the experiment. Monitoring the 384-well co-cultures over time by microscopy showed full adherence in all observed wells at low astrocyte numbers of 1000 seeded pA/well and for both coating conditions over the course of 3.5 weeks (10 of 10 replicate wells, Fig S1F,G). In contrast, for co-cultures with high astrocyte number up to all 10 replicate wells showed full detachment of cells from the well surface by d31. This effect was most prominent at highest total cell density (3’000 astrocytes and 25’000 neurons per well) with 9 and 10 out of 10 replicate wells detached for laminin and Geltrex coating, respectively. Overall, cell adherence was less vulnerable to changes in cellular composition in 96-well compared to 384-well format (not shown). These findings show that cell type composition determines cellular distribution and adherence and thus, may influence neural network development and function. They further underline the importance of careful monitoring of human CNS-cell co-cultures, particularly also in an automated environment and of building an understanding of how unexpected events affect various endpoint measurements. Given that coating conditions showed minor impact on above analyzed

culture parameters and, due to ease of handling, we performed subsequent experiments on Laminin, unless otherwise mentioned.

3.3 The cell type ratio determines network firing patterns.

GCaMP6f signal revealed network-wide firing properties of the various neuron-astrocyte co-culture conditions. Baseline neural network activity was recorded for 5 min, followed by acute treatment with neuroactive compounds and 5 min recording of the ensuing drug response over time. Recordings were performed in stimulating buffer conditions adapted from Sun and colleagues (Sun & Südhof, 2021) that enable spontaneous network oscillations. Baseline readings showed consistent network activity with various network spike frequencies and mean network spike amplitudes depending on the co-culture composition and culture format (Fig 1E,F). Overall, the frequency ranges in 96-well and 384-well plate formats were comparable, as were spike amplitudes, considering the differences in area and numbers of neurons contributing to the signal (Fig 1G,H). Analysis of network activity pattern revealed a major impact of neuron density on network spike frequency and amplitudes showing a negative correlation with the former (Pearson r of -0.72 and -0.64 for 96-well and 384-well plate, respectively) and a positive correlation with the latter (Pearson r of 0.65 and 0.71 for 96-well and 384-well plate, respectively, Fig 1 G,H). A similar impact was seen for total cell density and GLUT iN/pA cell type ratio. For the latter parameters, results may be explained largely by their strong dependence on the GLUT iN numbers, which exceeded the pA numbers considerably. The impact of pA density on network activity was less clear as a positive correlation of spike frequency with pA density found in the 384-well plate format (Pearson r = 0.38) was not detected in the 96-well plate (Pearson r = -0.073). There was a slight negative correlation of mean spike amplitude with pA density in the 96-well plate and in the 384-well plate format (Pearson r = -0.36 and -0.2, respectively). The overall negative correlation of spike frequency and amplitude across various seeded GLUT iN numbers is also highlighted by graphing of the two parameters at constant pA density (Fig S2 A). We repeated above experiments with additional GLUT iN/astrocyte ratios to further refine the cell type ratios and confirmed optimal seeding ratios of 15’000 GLUT iN and 2000 to 2500 pA for 384-well format and 90’000 to 100’000 GLUT iN to 10’000 pA for 96-well format plates (not shown). Further experiments were performed under these conditions, unless otherwise mentioned.

Next, we tested responses of our system to modulators of neuronal firing. First, we established that DMSO, a widely used dissolution agent, did not impact spike amplitude or frequency up to 0.3% (Fig 1 H), Next, we demonstrated that our neurons have functional voltage gated potassium channels (K_V), by using K_V antagonist 4-aminopyridine (4-AP), which increased spike frequency in a dose-dependent manner. KCNQ channel opener retigabine led to dose-dependent reduction in spike frequency (IC50 = 0.94µM), whereas the spike amplitude was not significantly reduced. GABA, the endogenous ligand for GABA receptors, produced a dose-dependent reduction in spontaneous neuronal activity (IC50 = 0.31µM) with only a small effect on calcium spike amplitudes (Figure 1H). Lastly, spontaneous neuronal activity was also looked at in the context of Neurobasal/B27 PLUS medium. However, these culture conditions failed to produce robust synchronized firing and their depolarizing response to GABA suggested an immature state of neural networks around 4 weeks in culture (Figure S2 C). These results reveal a major dependency of neural network firing on neuron astrocyte ratios, while two tested coating conditions did not show differential impact. Furthermore, the typical responses of the GLUT iN in our co-cultures with pA to modulators of voltage-dependent potassium channels, the hyper-polarizing effect of GABA suggest the presence of relatively mature, glutamatergic neuronal networks at the time of calcium measurements.

3.4 DAPT negatively impacts astrocyte viability.

Previous work used the γ-secretase/Notch-signaling inhibitor N-[N-(3,5-difluorophenacetyl)-L-alanyl]-S-phenylglycine t-butyl ester (DAPT) to promote conversion of precursor cells into postmitotic GLUT and GABA iN (Meijer et al., 2019; Rhee et al., 2019). Furthermore, chronic exposure to DAPT led to altered synaptic function in GLUT iN via changes in cholesterol metabolism, including evidence for enhanced excitatory synapse formation (Essayan-Perez & Südhof, 2023). We therefore wanted to test whether DAPT had a beneficial effect on our culture system with respect to neuronal maturation and/or synapse formation. Given evidence from previous observations and LDH measurements that the primary human fetal astrocytes continued proliferating in the days after seeding and prior to ara-C treatment, the actual cell type ratio post-ara-C treatment was not expected to match the original seeding ratios anymore. Therefore, we needed a method to precisely assess final cell numbers, ideally at cell-type resolution. We developed a method to assess the GLUT iN/pA ratio at the end of experiments by harnessing the different nuclear appearance of neurons and astrocytes (Fig 2A). In our cultures, neuronal nuclei were small, roundish, and stained brightly with DNA-intercalating dyes, while astrocyte nuclei were bigger, of elongated oval shape, and stained dimmer compared to neuronal nuclei (Fig S3A). Exploiting these features, we trained a learning algorithm, StarDist (Schmidt et al., 2018), for automated nuclei detection (Fig S3A) and quantified cell type ratios at d28, with and without acute DAPT treatment (10µM) at d4, similar to what was previously described. Acute treatment with DAPT at d4 resulted in a significant increase in neuron numbers (mean±std) by d28 compared to control (998.4 +/-196.3 /mm2 vs 752.4 +/-196.3 /mm2, p_{TTEST} = 8.24E-11). At a well area of 10.6276 mm^2 this translated to 71% and 53% GLUT iN survival at d28 compared to 15’000 GLUT iN seeded at d4 for DAPT treatment vs control, respectively. In turn, we were surprised to find a significantly lower number of astrocytes upon DAPT treatment compared to control (194.4/mm2 +/-45.1 vs 300.3/mm2 +/-64.4, p_{TTEST} =4.42E-21), which translated to 82.6% and 127.6% pA survival at d28, compared to 2500 pA seeded at d2. These numbers also led to the GLUT iN/pA cell-type ratios at d28 of 5.3 +/-1.5 and 2.6 +/-1.0 for DAPT-treated vs control cultures. Due to total cell density mainly determined by the more abundant neurons, the survival ratios, which we defined by the ratio between seeded cell density (pA at d2 and GLUT iN at d4) and the cell density at the end of the assay, were at 0.75 +/-0.12 and 0.66 +/-0.14 for DAPT-treated vs control cultures. Considering some degree of proliferation of pA between seeding at d2 and ara-C treatment starting at d7, a final GLUT iN/pA ratio ending up lower than the GLUT iN/pA ratio at seeding (d4/d2) was expected. In contrast, the final GLUT iN/pA ratio of 5.3 in DAPT-treated cultures, which came close to the seeding ratio of 6.0. We therefore tested whether the reduced pA numbers in DAPT-treated cultures (Fig 2E) resulted from interference of DAPT with proliferation, or whether or from death of pA. Realtime monitoring of pA monocultures in the presence of stain for apoptosis (caspase 3/7 stain, Fig 2D)) suggested that cell death is the main driver of this outcome. Furthermore, the timeline of the live-monitoring results suggested an immediate impact of DAPT on pA viability, which faded after 24 hours.

The addition of DAPT for 3 days to the culture medium resulted in changed firing patterns. Using both the genetically encoded calcium indicator GCaMP6f as well as the organic calcium dye Calcium-6 (Molecular Devices), we consistently observed a decrease in network spike amplitudes and an increase in network spike frequency (Fig 2F,G & Fig S3B,C). The presence of DAPT significantly reduced the mean frequency from 5.2±0.7 events/min to 2.2±0.7 network spikes/min for GCaMP6f (p_{TTEST} =1.66E-11) and from 3.2± 0.4 events/min to 0.9±0.3 network spikes/min for Calcium-6 (p_{TTEST} =8.75E-24). The exposure of our neuron-astrocyte coculture to DAPT resulted in a significant increase in mean calcium transient amplitude, namely from 322±58 RFU to 419±84 RFU for GCaMP6f (p_{TTEST} =0.026) and from 2664±462 RFU to 4059±341 RFU for Calcium-6 (p_{TTEST}

=2.30E-12). These changes in network firing of DAPT-treated cultures are largely consistent with what would be expected from changes in GLUT iN/pA ratios, as observed in our previous experiments. Therefore, DAPT impact on network firing is due likely to early loss of pA and increased survival of GLUT iN.

3.5 GABAergic inhibitory neurons increase the network spike frequency and reduce the amplitude.

Local GABAergic inhibition plays an important role in shaping the functional properties of neural networks across the brain, including via controlling local and global network excitability and synchronization. GABA-mediated inhibition may also contribute to network dysfunction in a variety of CNS disorders including epilepsy, autism, or schizophrenia. We therefore wanted to study the impact of GABA neurons on the in vitro human neural networks described above.

For exploring the effects of GABA-mediated inhibition in the context of the calcium oscillation assay, we engineered an iPSC line for reprogramming of GABA iN. We inserted a transgene for inducible expression the neurogenic transcription factors ASCL1 and DLX2, inducible over-expression of which was previously shown to efficiently reprogram iPSC into GABA iN, using lentiviral transduction or within a stable cell line (Rhee et al., 2019; Song et al., 2021; Yang et al., 2017), into a commercially available iPSC line. Furthermore, the insertion was carried out in the context of testing the usefulness of a more general approach for efficient introduction of any reprogramming code of interest into an iPSC line. For the latter, we equipped the iPSC with a constitutively active rtTA transgene and a tetracycline-responsive Cre recombinase fusion with nuclear EGFP in the ROSA26 and AAVS1 genomic loci, respectively. The transgenes further contained a combination of incompatible Lox sites recognized by Cre to enable recombinase-mediated cassette exchange and efficient insertion of reprogramming codes in place of the Cre-EGFP fusion coding sequence (Fig S4A)(Baer & Bode, 2001; Kolb, 2001; O'Gorman et al., 1991).

Following established reprogramming protocols, we generated GABA iN and grew them in co-culture on pA, with or without GLUT iN. Four weeks later, we collected cells from 384-well plates to perform multiplexed single-nucleus RNA sequencing (snRNA-seq) using cell multiplexing oligonucleotide (CMO) barcodes to track well origins. For analysis, we pooled data from 2 wells of GABA iN on pA, and 4 wells from co-culture also including GLUT iN. CMO labeling efficiency based on 80% confidence was at a relatively low 67%, suggesting that CMOs originally developed for labeling of the plasma membrane may benefit from future adaptations in the context of nuclear membrane properties. In total, 564 nuclei could be traced back to specific wells of origin. After removal of multiplets and droplets with low signal, visualization in a T-SNE plot distinguished three major cell types matching a total of 124 GABA iN, GLUT iN, and pA (Fig 3B). The distinction is further visualized by clustering based on characteristic marker gene expression (Fig 3C). Generally, neurons were identified by expression of genes encoding synaptic components (*HOMER1*, *UNC13*, *SYN2*, *GPHN*), cytoskeleton (*MAP2*), neuron-enriched transcription factors (*RBFOX3*, *CUX1*, *CUX2*). In contrast, the pA transcriptome was enriched for markers of their fetal origin in the forebrain (*FOXG1*), of typical extracellular matrix proteins (collagen genes) and cytoskeletal components (*VIM*), as well as of surface receptors (*CD44*). GLUT and GABA iN differentially expressed surface receptors (*GRM8*, *RYR2*), transcription factors (*EBF1*, *RBFOX1*), and genes playing a role in their respective neurotransmitter metabolism (*GAD1*, *GAD2*) and transport (SLC17A6 versus SLC32A1, respectively). Immune-cytochemistry further confirmed enrichment of GABA in GABA iN versus GLUT iN (Fig 3D). At the level of qualitative cell culture properties, the addition of GABA iN reduced the tendency of GLUT iN to form clusters (Fig 3E). Nuclei counts at

d28 confirmed increased neuron numbers upon addition of GABA iN, as expected (1294.0 +/-195.2 /mm2 vs 752.4 +/-196.3 /mm2, p_{TTEST} = 2.36E-14). However, the degree of increase in the presence of GABA iN (+72% compared to control) was higher than expected based on the seeding ratios (total 20000 vs 15000 neurons per well or +33.3%). Along the same lines, we observed a significantly higher density of pA in the presence of GABA iN (360.6/mm2 +/-64.2 vs 300.3/mm2 +/-64.4, p = 0.008), a plus of 20% compared to control. These higher-than-expected numbers were further reflected in a higher survival ratio in the presence of GABA iN (0.80 +/-0.12), compared to control (0.66 +/-0.14) co-cultures. Overall, the apparent positive effect of GABA iN on cell numbers for both neurons and pA, led to final iN/pA ratios of 3.6 vs 2.6 in presence vs absence of GABA iN. This 38% increase roughly matched again the expected 33.3% increase based on the initial number of GABA iN seeded. These results suggest that addition of GABA iN to the co-culture of GLUT iN and pA has an overall positive effect on cellular distribution and viability.

The addition of GABA iN resulted in an increase in network spike frequency (0k iGABA vs 5k iGABA neurons: 6.4+/-1 spikes/min vs 9+/-1.4 spikes/min, p_{TTEST} = 3.38E-14) and a decrease in calcium spike amplitudes (0k iGABA vs 5k iGABA neurons: 335+/-82 RFU vs 215+/-35 RFU, p_{TTEST} = 3.27E-08) compared to co-cultures without GABA iN (Fig 4 H). This effect of the presence of GABA iN was reverted when the GABA receptor antagonist bicuculline was added (Fig S6 A+B), indicating that the observed changes were indeed mediated by GABA.

3.6 Altered neural network activity and reduced synchronization of local field activity in the presence of GABA iN.

The increase in GLUT iN network spike frequency observed in the presence of GABA iN, despite having been reported in a similar assay based on fetal rat CNS cells (Xing et al., 2021), is not easily reconciled with GABA-mediated inhibition usually decreasing neuronal excitability. The previous study in rat neuron cultures proposed that GABA-mediated increase in network firing frequency involves reduced synchronization of local firing activity. The resulting decrease of participation of local firing in network spikes could therefore also explain the decreased network spike amplitude we observed in the presence of GABA iN in our human in vitro system. (Fig 3 H). To further explore this and to assess the observed calcium signals at subnetwork-level, we took to analyzing our plate-reader data at pixel-resolution. This approach turned each pixel into a sensor for local field calcium activity, similar to electrodes in a multi-electrode array (MEA) measuring local field activity based on extracellular voltage-changes. Co-cultures of 90’000 GLUT iN and 10’000 pA, with and without 30’000 or 60’000 GABA iN were grown in a 96-well format. After recording calcium signals, the gray-scale movies from the plate reader were overlaid with a grid-mask and pixels covering a slightly larger area than the actual growth area of the wells, due to angular distortion arising from the camera perspective (Fig S5 A). The growth area was estimated based on the autofluorescent signal from dry border wells. Clustering of pixel brightness thus allowed to define growth area, a border zone, and an outside area (Fig S5 B). A conservative estimate of the growth area excluding the well border area yielded a coverage of about 400 pixel per well (Fig S5 C). This number yields an upper estimated area coverage per pixel of 80425 μm^2 (~284 x 284 μm) and, integrated with the mean cell type-specific nuclei counts from this co-culture of GLUT iN (1307 +/-123) with pA (331 +/-21), a mean of 105 GLUT iN and 25 pA covered per pixel.

We focused subsequent analyses on the 400 “most active” pixels based on the top-400 mean maximum spike signal, similar to focusing MEA data analysis on “active” electrodes. Heat maps of the top-400 pixels reflected the network spike pattern measured on average across the well (Fig 4 A). In addition, they revealed a multitude of un-coordinated local field spikes for each pixel’s location.

The presence of GABA iN in the co-culture again increased the frequency of network spikes (from 3.3 +/-0.4 without GABA iN, to 5.4 +/-0.7 spikes/min, p_{TTEST} = 0.004, and to 4.3 +/-1.5, n.s., with 30’000 and 60’000 GABA iN, respectively), and reduced their amplitude (from 1598.6 +/-51.7 without GABA iN, to 1048.2 +/-41.5 RFU, p_{TTEST} = 7.29E-7, and to 853.9 +/-152.4 RFU, p_{TTEST} = 6.57E-5, with 30’000 and 60’000 GABA iN, respectively) (Fig S5 E). However, this pattern was not followed at the level of (pixel) spikes reflecting local field activity (Fig 4 C). The mean spike frequency of all pixels of a well (averaged across N = 5 wells) showed a tendency to be decreased by 30000 GABA iN and was unchanged by 60000 GABA iN by the presence of GABA iN (5.6 +/-0.9 without GABA iN, versus 4.2 +/-0.6 spikes/min, n.s., and versus 5.7 +/-0.7 spikes/min, n.s., with 30’000 and 60’000 GABA iN, respectively). The mean amplitude of local spikes averaged across wells showed a minor, though significant reduction by the presence of GABA iN (from 0.48 +/-0.005 without GABA iN, to 0.46 +/-0.002 RFU, p_{TTEST} = 4.16E-4, and to 0.46 +/-0.006 RFU, p_{TTEST} = 0.01, with 30’000 and 60’000 GABA iN, respectively). However, the magnitude of amplitude change of local spikes was far from the magnitude of change observed for network spikes (compare Fig 4 C and Fig S5 D, E). In addition, the full width at half maximum (FWHM), which is spike width at half height, was reduced in the presence of GABA iN, reaching significance with 60’000 GABA iN, and possibly reflecting a shortened burst length (from 597.9 +/-38.0 without GABA iN, to 473.1 +/-9.0 ms, n.s., and to 394.6 +/-37.5 ms, p_{TTEST} = 0.015, with 30’000 and 60’000 GABA iN, respectively).

To investigate whether there is a potential difference of GABA iN-mediated changes to local field activity depending on whether such local field activity coincides with network activity or not, we divided the spikes of each pixel into those participating in a network spike (further termed IN spikes), and those that fell outside network spikes (OUT spikes)(Figure 4 D-E). The mean spike amplitude across wells was significantly higher for IN spikes than compared to OUT spikes (without GABA iN: 0.52 +/-0.01 versus 0.45 +/-0.003 RFU, p_{TTEST} = 1.51E-5, with 30’000 GABA iN: 0.47 +/-0.003 versus 0.45 +/-0.002 RFU, p_{TTEST} = 1.33E-6, with 60’000 GABA iN: 0.48 +/-0.007 versus 0.46 +/-0.002 RFU, p_{TTEST} = 8.64E-4)(Figure 4 F). And interestingly, GABA iN only reduced the mean spike amplitude of inside spikes (from 0.52 +/-0.01 without GABA iN, to 0.47 +/-0.003 RFU, p_{TTEST} = 3.48E-4, and to 0.48 +/-0.007 RFU, p_{TTEST} = 1.86E-3, with 30’000 and 60’000 GABA iN, respectively), but not outside spikes, which were even slightly higher in presence of 60’000 GABA iN (from 0.45 +/-0.003 without GABA iN, to 0.45 +/-0.002 RFU, n.s., and to 0.46 +/-0.002 RFU, p_{TTEST} = 0.043, with 30’000 and 60’000 GABA iN, respectively). Similarly the FWHM was higher for IN spikes compared to OUT spikes (without GABA iN: 720.7 +/-19.5 versus 340.6 +/-0.76 ms, p_{TTEST} = 8.36E-10, with 30’000 GABA iN: 617.4 +/-16.9 versus 347.8 +/-3.4 ms, p_{TTEST} = 4.98E-9, with 60’000 GABA iN: 546.5 +/-29.8 versus 345.3 +/-1.0 ms, p_{TTEST} = 3.66E-6)(Fig 4 F), and selectively reduced by the presence of GABA iN (from 720.7 +/-19.5 without GABA iN, to 617.4 +/-16.9 ms, p_{TTEST} = 1.92E-4, and to 546.5 +/-29.8 ms, p_{TTEST} = 4.30E-5, with 30’000 and 60’000 GABA iN, respectively). For the OUT spikes, the presence of GABA iN even slightly increased the FWHM (from 340.6 +/-0.76 ms without GABA iN, to 347.8 +/-3.4 ms, p_{TTEST} = 0.017, and to 345.3 +/-1.0 ms, p_{TTEST} = 3.6E-4, with 30’000 and 60’000 GABA iN, respectively), reaching significance due to an order-of-magnitude smaller variability for OUT spikes compared to IN-spike FWHM. The lower variability of OUT spikes across wells may be explained by OUT spiking activity largely depending on intrinsic firing properties of the highly homogeneous NGN2-reprogrammed neurons,

while the IN spikes are likely to be shaped also by the complex network architecture that may vary more across wells compared to intrinsic neuronal firing properties. The decreased the FWHM for the IN spikes in presence of GABA iN is in line with the observation by (Mossink et al., 2022), who show similar effects for network burst duration using MEA recording, thus demonstrating the power of our imaging-based method despite comparably lower temporal resolution. Given that spike detection is dependent on amplitude and prominence threshold applied, we also quantified the fraction of spikes detected across thresholds starting to measure threshold-dependent loss of IN spike versus OUT spikes in the presence or absence of GABA IN (Fig 4 G, H). We defined a prominence threshold of 0.1, which is just outside of high-intensity noise as defined above (Fig S5 G,H), as 100% of spikes detected. This analysis revealed that with increasing spike detection thresholds, IN spikes were lost earlier in the presence of GABA iN compared to GLUT iN co-cultures only, while OUT spikes were not affected (Fig 4H). This result is consistent with the above mentioned decrease of spike amplitude at a fixed detection threshold in the presence of GABA iN, selectively observed for IN spikes and is suggestive of a decreased participation of local field activity in synchronized network activity.

Finally, we harnessed the pixel-based analysis of calcium signals to take a look at network synchronization. The pair-wise correlation of activity patterns for all pixels was calculated and clustered heatmaps created. The presence of GABA iN reduced the correlation coefficients for pairs of pixels and this effect was observed in a GABA iN density-dependent manner (Fig 4I). Adding the distance between pixels based on each pixel's coordinates on the plate image further allowed for visualization of synchronization in dependence of distance across the network. This analysis showed that the pair-wise correlation coefficients of pixel activity are lower across the well surface in the presence as compared to absence of GABA iN. All together these findings indicate that GABA iN have a major impact on the spike properties of local field activity when it participates in synchronized network activity (IN spikes), as opposed to local field activity not participating in network spikes. In addition, GABA iN generally reduce synchronization of local field activity across the well.

3.7 Effects of GABA iN on GLUT iN network activity are mediated by GABA signaling.

Finally, we tested whether the impact of GABA iN on GLUT iN network activity is indeed mediated by GABA. For this, we treated co-cultures of GABA iN, GLUT iN, and pA with bicuculline, a competitive antagonist of GABA A receptors. In co-cultures of 90'000 GLUT iN, 10'000 pA, and 30'000 GABA iN, recording of baseline activity at d31 for 5 minutes was compared to 5 minutes of subsequent activity in the presence of 5 µM bicuculline. Bicuculline treatment significantly increased the network spike amplitude compared to baseline control (927.5 +/-15.1 vs 729.8 +/-22.4 RFU, p_{TTEST} = 1.60E-5), and showed a tendency to decrease the mean network spike frequency compared to control (2.57 +/-0.33 vs 2.95 +/-0.55 network spikes/min, n.s.)(Fig S6 A,B).

For local field activity measured at pixel-resolution the mean spike amplitude and the mean FWHM were significantly increased by bicuculline as compared to baseline control (mean spike amplitude: 0.53 +/-0.01 vs 0.50 +/-0.009 RFU, p_{TTEST} = 0.012; mean FWHM: 666.8 +/-41.8 vs 603.1 +/-46.8, p_{TTEST} = 7.33E-4), while the mean spike frequency showed a tendency towards being reduced (0.76 +/-0.52 vs 0.80 +/-0.49, n.s.), (Fig 5A,B). Isolated analyses of IN and OUT spikes showed that

bicuculline selectively increased the mean IN spike amplitude compared to baseline control (0.621 +/-0.007 vs 0.557 +/0.009 RFU, p_{TTEST} = 4.57E-5), while no effect was detected for OUT spikes (0.444 +/-0.002 vs 0.448 +/-0.002 RFU, n.s.) (Fig 5 C). Similarly, the mean FWHM was selectively increased by bicuculline compared to baseline control (997.4 +/-69.8 vs 881.8 +/-89.4 ms, p_{TTEST} = 2.42E-3), while it was even slightly decreased for OUT spikes (325.1 +/-4.1 vs 337.8 +/-4.9 ms, p_{TTEST} = 1.98E-3). Bicuculline further increased the pairwise correlation between activity patterns of all pixels and across distances, suggesting increased synchronization of calcium activity across the well (Fig 5 E). No significant changes were detected by the addition of the vehicle DMSO for any of above-mentioned parameters (Fig S6 E,F). Furthermore, measurements of GABA concentration in the medium across various timepoints of the assay confirmed increased GABA levels in co-cultures of GLUT iN and pA with GABA iN as compared to without (two-way p_{ANOVA} = 2.61E-6), as well as over time of culture (two-way p_{ANOVA} = 2.34E-8), including interaction between the two (p = 4.72E-3) (Fig S6, H).These experiments with the GABA A receptor antagonist bicuculline showed overall opposite effects to those seen by adding GABA iN to the co-cultures of GLUT IN and pA. The findings therefore suggest that effects on GLUT iN network activity as well as on synchronization of local field activity by addition of GABA iN to the co-culture are indeed mediated by the action of GABA.

4 Discussion

This study set out to develop a calcium oscillation assay based on co-culture of human excitatory neurons and astrocytes towards scalable applications suitable for high-throughput compound screening. As cellular model for excitatory neurons we chose NGN2-reprogrammed GLUT iN derived from human iPSC. Primary fetal astrocytes, pA, provided support for neural network development. The assay was optimized to be compatible with regular weekday working schedules and automated liquid handling.

Our data show that the ratio of astrocytes and neurons affects cell adhesion and distribution on common HTS-compatible optical plates and furthermore, that they shape neural network activity as measured by calcium entry into the neurons. The GLUT iN in our co-cultures with pA display a typical response pattern to modulators of key neuronal ion channels including voltage-dependent potassium channels, as well as GABA receptors, suggesting a degree of maturity to serve as functional in vitro models of human excitatory neuron types. The assessment of DAPT, a γ-secretase/Notch-signaling inhibitor, for previously reported promotion of cell cycle exit and maturation of GLUT and GABA iN as well as modulation of synapse formation, was interfered by the compound's negative impact on astrocyte viability, thus altering the cell type ratios of the co-culture system. In this context and to properly compare seeded ratios of astrocytes and neurons at d2 and d4, respectively, with their ratios at the time of functional measurements, an image-based quantification method was developed that takes advantage of the different appearances of astrocytic and neuronal nuclei when stained with nuclear dyes. We finally show that the addition of inhibitory GABA iN to the co-culture system affects neural network firing patterns. However, surprisingly, the GABA iN effect was selective to network spikes and not detected on local calcium spiking temporally independent of synchronized network activity. In order to achieve this, we developed the analysis of plate reader-based calcium oscillation data to retain pixel-resolution rather, thus turning the signal from each pixel into a local field calcium recording.

While it is generally agreed that the formation of functional human neural networks in vitro depends on signals from astrocytes to promote synapse formation and maturation, examples of scalable drug discovery assays based on such human neural networks are still sparse (Bassil et al., 2021; Patzke et

al., 2015; Saavedra et al., 2021; Shan et al., 2024). Our work shows that development of such scalable assays is complicated by several factors, including timelines for maturation of neurons, development of neural networks, continued astrocytic support, uncertainties about the cell type ratios in a two-dimensional culture setup, and an incomplete mechanistic understanding of how cellular activity generates synchronized activity of an entire neural network. Our work emphasizes the importance of careful assessment of the ratio of neurons and astrocytes, not just when seeding the cells, but also at the time of functional endpoint measurements. It further adds to the growing toolbox for precise quantification of neurons and astrocytes in such assays by means of differentiating these two cell types based on their nuclear appearance after fluorescent staining. In principle, our nuclei-based cell type quantification is applicable both to fixed and live-stained cultures, thus enabling real-time monitoring of neuron-to-astrocyte ratios in the future.

Inclusion in the assay protocol of factors that are commonly thought to promote neuronal network maturation, such as DAPT, may need careful testing for their effects on other cell types. Here we show that even a 24-hour exposure to DAPT has dramatic consequences for astrocytic support due to a negative effect specifically on the viability of the pA, in contrast to GLUT iN. The Notch signaling pathway is an important regulator of cell proliferation and maturation. Therefore, while an impact on remaining proliferative activity of astrocytes might have been expected by pharmacological modulation of Notch signaling, it came as a surprise that our data suggest a major impact on cell viability. Therefore, the herein reported effect of DAPT may merit further exploration particularly if the compound's proposed positive effects on neuronal maturation want to be exploited in such human in vitro calcium oscillation assays.

At the network activity level, our data largely showed that GABA iN, somewhat counterintuitively, increase the frequency of network spikes while reducing the network spike amplitude. This is in line with a similar study using co-cultures of excitatory and inhibitory neurons (Xing et al., 2021). However, while the electrode readout from MEA has a temporal resolution for isolation of single action potentials from a local field, it is unable to resolve cell type-specific contributions to the observed synchronized network activity. The imaging-based approach we took here, while resolving activity patterns only at the level of action potential bursts, is able to selectively provide signals from the GLUT iN population in the networks, due to cell type-specific expression of the calcium indicator GCaMP6f. Furthermore, we enabled the measurement of local field calcium activity by extracting and analyzing fluorescence intensity data from the plate reader at pixel resolution. This approach enables coverage of local calcium activity with a conservatively estimated 400 pixels per well of a 96-well plate, with the potential for scaling to 384-well format at an estimated coverage of roughly 130 pixels per well for the optical plates used herein (giving or taking of the well boundary area, as described in Figure S5B, which may also differ between round and square shaped wells). These metrics surpass most current MEA formats both in spatial coverage and available well-replicate numbers per plate. Using pixel-resolution data to assess local field calcium activity, we found evidence that GABA iN-mediated inhibition is largely restricted to synchronized network-level neuronal activity, while sparing locally confined calcium spikes that do not coincide with network spikes. The observation that with addition of GABAergic neurons to the co-culture, the number of spikes participating in synchronized activity (IN spikes) is decreased (fig 4H), is consistent with findings by Xing and colleagues (Xing et al., 2021). Furthermore, the decreased FWHM for the IN spikes in presence of GABA iN is in line with the observation by Mossink and colleagues (Mossink et al., 2022), who show similar effects for network burst duration using MEA recording, thus demonstrating the power of our imaging-based method despite comparably lower temporal resolution. Nevertheless, while GABA's impact on spike shape-related parameters of local field activity, such as amplitude and FWHM, was detected for IN spikes (i.e., during network-wide

spiking), without detectable change for OUT spikes, GABA iN also affected the overall synchronization of local field activity, as shown by correlation analysis. This suggests that in these co-cultures of GLUT and GABA iN with pA, a major role of GABA iN is to control the distribution of local GLUT iN activity and its participation in synchronized network activity. To what extent our findings have implications for our understanding of GABA action and neural network synchronization in vivo, including in epilepsy, autism, schizophrenia or other conditions, remains to be seen.

In conclusion, this study contributes to developing functional neural network assays based on human CNS cell types, and to facilitating their application in scalable drug discovery environments. This is of particular relevance in light of initiatives by regulatory agencies, including the FDA Modernization Act 2.0, gaining traction in drug discovery research to increasingly complement and, where possible, replace animal models with human cellular model systems (Zushin et al., 2023). The work highlights key parameters to be considered when establishing calcium imaging assays to study human neural network function in vitro, and methods to reconcile scaling of optical calcium measurements by microplate reader with a level of resolution enabling the recording of local field activity similar to MEA systems. A major limitation to generalization of this and similar assay protocols remains the primary tissue origin astrocytes, which play a critical role in development and function of neural networks. Anatomical origin as well as preparation inevitably result in batch-specific properties of pA. The replacement of primary cells to build fully iPSC-derived assays of unlimited cellular sourcing should therefore become a primary focus of future research. Protocols for reprogramming iPSC into astrocytes (iA) have been reported and thus offer a promising starting point in this direction (Canals et al., 2018). Fully renewable sourcing of cells is of particular importance for scalability and automation of assays in drug discovery applications.

5 Conflict of Interest

All authors are or were at the time of the study employees of Idorsia Pharmaceuticals Ltd.

6 Author Contributions

Conceptualization (TP), Data curation (MDH, TP), Formal analysis (MDH, TP), Investigation (CD, SS, LL, JM, EG, LT, PB, BR, SB, SW), Methodology (MDH, TP), Project administration (TP), Software (MDH, TP), Supervision (MDH, EG, PB, TP), Validation (MDH, TP), Visualization (MDH, TP), Writing – original draft (TP), Writing – review & editing (MDH, CD, SS, LL, JM, EG, LT, PB, BR, SB, SW, TP).

7 Acknowledgments

We thank John Fuller and Bruno Sempère for help with the implementation of nuclei quantification by StarDist, and Diego Fernandez and John Fuller for help with initial versions of network spike detection using Python.

8 Data Availability Statement

The snRNA-seq data will be made available at GEO.

9 Figure Legends

Figure 1. Development of an all-human invitro calcium oscillation assay. A) Schematic overview of calcium assay. Media types, key ingredients, and schedule of media renewal are underlaid gray. Time is denoted as day (d) in culture starting with single-cell seeding of iPSC. B) Confocal images at d31, from left: bright-field, GCaMP6f (maximum intensity projection of 60 sec calcium imaging at 4 fps), RFP, Hoechst nuclear (live) stain, to right: merged fluorescent channels. Scale bar = 100 μm. (C-D) Circular super-clustering of GLUT iN in 384-well co-culture, in dependence of pA seeding density (C), and GLUT iN seeding density (D). Scale bars = 500 μm. (E-F) Excerpt of baseline traces for increasing GLUT iN seeding density at fixed pA density in 96-well (E) and 384-well (F) culture formats visualize the dependence of firing patterns on GLUT iN numbers. Signal correction: SU spatial uniformity. (G-H) Dependence of network spike frequency (left) and mean network spike amplitude (right) on GLUT iN seeding density, at fixed pA seeding densities of 10'000 and 1000 per well as in 96-well (G) and 384-well (H) culture formats, respectively. Only wells with fully adherent cells were included in the analysis. N= 4 wells for each neuron density (G) and 10 wells each (H), respectively. I) Drug treatment reveals concentration-dependent effects of modulators of neuronal activity. Neither network spike frequency (top row) nor network spike amplitude (bottom row) are changed in the presence of up to 0.3% DMSO. The opposing effects of potassium channel blocker 4-aminopyridine (4-AP) as well as the K_V7 opener retigabine demonstrate that iNs have fully functional voltage-gated potassium channels. Increasing concentrations of GABAR ligand GABA lead to a dose-dependent block of spontaneous neuronal activity. (N= 3 wells per compound concentration). Boxplots denote 2nd and 3rd quartile (gray), with bars extending to 1.5 times of the IQR. Individual datapoints are overlaid as dots.

Figure 2. Impact of DAPT on co-culture of GLUT iN with pA. A) Fluorescence microscope images illustrate the different nuclear appearance (Hoechst nuclear stain) of iN (identified based on RFP expression) and pA (identified based on expression of astrocyte marker SOX9). Scale bar = 20 μm. B) Quantification of GLUT iN (left) and pA (right) based on cell type-specific nuclear appearance. C) The final iN-to-pA was calculated (left), as well as the survival ratio as defined by total cell number at the end of the assay compared to total number of seeded cells. N=80 wells per group. (D-E) Confluence of pA mono-culture (D) and activated Caspase 3/7 area (E) with DAPT treatment and without. N = 3 wells per condition, Error bars denote the 95 % confidence interval. F) Impact of DAPT treatment on neural network activity as measured by GCaMP6f. N= 15 wells per condition. Boxplots denote 2nd and 3rd quartile (gray), with bars extending to 1.5 times of the IQR. Individual datapoints are overlaid as dots. G) Relationship of network spike frequency and mean network spike amplitude shown in B, with and without DAPT treatment *$p<0.05$, ***$p<0.001$.

Figure 3. GABA iN affect GLUT iN neural network development and activity. A) Schematic view of genomic landing pad in the AAVS1 locus of the master iPSC line. The Cre recombinase (CRE), connected to nuclear (n) EGFP via a P2A sequence and under control of a tetracycline-sensitive promoter (Tet-ON), is expressed upon treatment with doxycycline. In the presence donor DNA harboring matching incompatible Lox sites, Cre recombinase-mediated cassette exchange (RMCE) inserts the Lox-flanked donor sequence to replace the Cre transgene. Selection is enabled via a CAGGS promoter included in the donor sequence to drive expression of a blasticidin S-resistance coding sequence (*bsr*). (B-C) snRNA-Seq of GABA iN, GLUT iN, and pA from d29 co-culture. 2-dimensional T-SNE projection showing the separation of cell types (B), and unsupervised clustering based on cell type-specific marker genes (C). D) Immune-fluorescence staining for GABA in a co-culture of GABA iN, GLUT iN (RFP positive), and pA. Scale bar = 20 μm. E) Cellular distribution of 384-well co-cultures with 15000 GLUT iN and 2500 pA, in the presence and absence of 5000 GABA iN. Total cells are shown visualized by bright-field (top). GLUT iN are visualized based on their RFP expression (bottom). F) Quantification of neurons (combined GLUT and GABA

iN) (left) and pA (right) based on cell type-specific nuclear appearance in 384-well co-cultures of 15’000 GLUT iN and 2500 pA with or without 5000 GABA iN . G) The final iN-to-pA was calculated (left), as well as the survival ratio as defined by total cell number at the end of the assay compared to total number of seeded cells. N=80 wells with GLUT iN and pA only. N=20 wells including 5000 GABA iN per well. H) Calcium imaging of GLUT iN in the presence and absence of GABA iN. Network spike frequency (left) and mean network spike amplitude (right) are shown. I) Scatterplot to visualize the relationship of network spike frequency and mean network spike amplitude in presence and absence of GABA iN. Boxplots denote 2nd and 3rd quartile (gray), with bars extending to 1.5 times of the IQR. Individual datapoints are overlaid as dots. **p<0.01, ***p<0.001.

Figure 4. GABA iN impact coincides with GLUT iN network spikes. A-B) Turning well-based plate reader data into pixel array data for analysis of local field activity in 96-well co-cultures of 90’000 GLUT iN and 10’000 pA, with or without 30’000 GABA iN: Normalized GCaMP6f fluorescence intensity heatmaps of the top-400 active pixels over time (bottom). Trace of the average signal reveals the network spikes (top) in absence (A) and presence (B) of GABA iN in the co-culture. C) Spike frequency (top), mean spike amplitude (middle), and mean full width at half maximum (FWHM, bottom). N = 5 wells, with 400 pixels averaged per well. For pixel-based graphs, see Figure S5G. D-E) Pixel-resolution calcium activity around single network spikes (marked with black arrowhead in A and B) in absence (D) and presence (E) of GABA iN. Traces of all top-400 active pixels are shown. Black line: mean signal across pixels, transparent red diamonds: Local area (pixel) spikes coinciding with a network spike (IN spikes), black transparent diamonds: spikes that fall outside of network spikes (OUT spikes). F) Mean spike amplitudes (top) and full width at half maximum FWHM (bottom) as separately analyzed for IN spikes and OUT spikes. G) Visualization of spikes and their coincidence with network spikes at two different detection thresholds, 0.2 (left) and 0.4 (right). For illustration purposes, the calcium trace of a single pixel is shown in yellow with yellow arrow heads denoting IN (large arrowhead) and OUT (small arrowhead) spikes. H) Spike detection in dependence of threshold and shown as fraction of total defined at a low threshold of 0.1 (close to noise, as defined in Fig S5H-I), for IN spikes (left) and OUT spikes (right). I) Clustered heatmaps of Pearson correlation coefficients for pair-wise correlation of pixel activity. J) Dependence of pair-wise pixel activity on distance as a measure for spreading and synchronization of local field activity within the well. Box plots denote 2nd and 3rd quartile (gray), with bars extending to 1.5 times of the IQR. Individual datapoints are overlaid as dots. Line plots show the 95% confidence interval around the mean as semitransparent area. *p<0.05, **p<0.01, ***p<0.001, n.s. = not significant.

Figure 5. GABA A receptor inhibition reverts effects of GABA iN on GLUT iN activity. A) Heatmaps of GCaMP6f fluorescence intensity for the top-400 active pixels for d31 co-culture of 90’000 GLUT iN, 10’000 pA, with 30’000 GABA iN recorded at baseline (top) and in presence of 5uM GABA A receptor antagonist bicuculline (bottom). (B) Spike frequency (left), full width at half maximum (FWHM, middle), and spike amplitude (right) at baseline and after bicuculline addition. (C) Mean spike amplitude (left) and FWHM (right) of spikes in dependence of network spike participation (IN versus OUT spikes). D) Spike detection in dependence of threshold and shown as fraction of total defined at a low prominence threshold of 0.1 (close to noise, as defined in Figure S5H-I), for IN spikes (left) and OUT spikes (right). The fraction of spikes was calculated for increasing prominence thresholds at a resolution of 0.01 threshold steps. E) (Pair-wise correlation of pixel intensities over time in dependence of distance between pixels, at baseline and in presence of bicuculline. N = 5 wells per condition, Box plots denote 2nd and 3rd quartile (gray), with bars extending to 1.5 times of the IQR. Individual datapoints are overlaid as dots. Line plots show the

95% confidence interval around the mean as semitransparent area. *p<0.05, .**p<0.01, ***p<0.001, n.s. = not significant.

Figure S1. Development of an all-human invitro calcium oscillation assay: culture conditions. A) Genotyping data for the genome-edited ROSA26 locus of the BIONi010-C13 neurogenic iPSC line. Schematic view of DNA construct and primer (blue arrows) alignment sites are shown. Top gel: 5-prime integration site, bottom gel: 3-prime integration site. P: parent cell line BIONi010-C13, W: water control, C: isolated clones (sample including positive and negative). The clone expanded for complete QC and use in experiments is denoted in bold font. For primer sequences, see Table S1 B) Early reprogramming phase (d0-d4) monitored by light microscopy at increasing magnifications. Scale bar = 100 μm. C) Relationship of LDH activity and cell type composition in a 96-well co-culture before (d7) and after Ara-C treatment, on Laminin (left) and Matrigel (right). Data is normalized on d7 baseline LDH activity. N = 5 wells per condition. Error bars denote the 95% confidence interval around the mean. D) Monitoring of RFP expression over time (top to bottom) for cellular distribution and surface adherence. Blue rectangle marks the determined optimal condition. E) Development of circular super-clustering of GLUT iN in over time in 96-well co-culture at pA seeding density of 2000/well. (F) Qualitative scoring of cellular adherence. G) Quantification of cellular adherence based on qualitative scoring for 384-well co-cultures grown on Laminin (left) and Geltrex (right). Scale bars E-F: 500 μm.

Figure S2. Development of an all-human invitro calcium oscillation assay: calcium imaging. A) Relationship of network spike frequency and mean network spike amplitude across a range of GLUT iN seeding densities at fixed pA seeding densities of 10’000 (left) and 1000 (right), in 96-well and 384-well co-culture formats, respectively. Only wells with fully adherent cells were included in the analysis. N= 4 wells for each neuron density in 96-well plate wells (left) and N = 10 wells for each neuron density in 384-well plate wells (right). B) Example trace of Ca^{2+} imaging shows that GABA (10µM, red trace) blocks spontaneous neuronal activity (black) in iNs grown in neurobasal A cell culture medium. C) iNs grown in Neurobasal Plus do not show spontaneous activity (black) and addition of GABA (10µM, red) leads to big increase in intracellular Ca2+, indicating that GABA acts in a excitatory, rather than inhibitory manner in these iNs. D-E) Concentration-response-curves calculated from the data in Fig 1I show that the 384-well plate format is suitable for testing the effects of compounds on spontaneous neuronal network activity in a high-throughput manner that is needed in drug discovery (N= 3 wells per compound concentration).

Figure S3. Impact of DAPT on co-culture of GLUT iN with pA. A) Representative image of Hoechst nuclear staining of neuron-astrocyte co-culture (left) and with mask for nucleus detection and counting using StarDist (right). The green outline denotes astrocytic nuclei, purple outline neuronal nuclei. Scale bar = 20µm. B) Network spike frequency and mean network spike amplitude as measured by Calcium 6 dye. N = 21 wells per condition. C) Relationship of network spike frequency and mean network spike amplitude shown in B, with and without DAPT treatment. Boxplots denote 2nd and 3rd quartile (gray), with bars extending to 1.5 times of the IQR. Individual datapoints are overlaid as dots. ***p<0.001.

Figure S4. Master iPSC line and recombinase-mediated cassette exchange. A) Schematic view of the modified *AAVS1* locus in the master iPSC line. The locus enables insertion of any reprogramming code by recombinase-mediated cassette exchange (RMCE) of donor DNA sequences flanked by incompatible Lox sites that match the Lox sites integrated in the genomic landing pad. Cre is expressed upon doxycycline treatment. Removal of the puromycin N-acetyltransferase (*pac*) selection cassette successful modification of the landing pad was enabled by compatible Lox sites

targeted and Cre upon doxycycline exposure in the absence of donor DNA. Nuclear (n) RFP under a constitutive promoter was used for proof-of-concept RMCE, replacing nEGFP. Promoters are shown as arrows: Tet-ON (black), PGK (orange), CAGGS (light gray), CAG (dark gray). Primer binding sites are shown as arrowhead in the colors matching subsequent figure panels. B) Genotyping data documenting the correct 5' and 3' integration of the genomic landing pad. C) Schematic view (top) and genotyping results (middle and bottom) for a CAGGS promoter-driven reverse Tet transactivator (*rtTA*) transgene to enable doxycycline-induced gene expression from the Tet-ON promoter. Selection for the modified ROSA26 locus was enabled by a blasticidin S-resistance gene (*bsr*) that was flanked by compatible Lox sites to enable removal upon doxycycline-induced expression of Cre recombinase. Genotyping results documenting the correct 5' (middle) and 3' (bottom) integration of the genomic landing pad after removal of the *bsr* cassette (dashed outline). D) Pluripotency marker analysis by immunefluorescence on the master iPSC line. E) Proof-of-concept RMCE: replacement of nEGFP by nRFP by RMCE. Master iPSC were treated with doxycycline for 24 hours before electroporation with the RFP-carrying donor DNA (see also (A) for schematic). Cells were treated for another 24 hours after 7 days of recovery to visualize both the recombined (red) and un-recombined (green) cells. F) DNA gels documenting the insertion of Donor DNA by RMCE. Primer (arrowhead) colors matching schema in (A). Clones indicated by large arrowheads: nRFP proof-of-concept RMCE clone (red), neurogenic iPSC clone used for generation of GABA iN (white). Scale bars = 50 μm.

Figure S5. Pixel-resolution plate reader measurements for analysis of local field calcium activity. A) Excerpt of a plate reader image of a 96-well plate overlaid with a mask for automated selection of regions of interest (ROI). ROI cover a bigger area than the actual well bottom to ensure coverage of the entire growth area independent of well position and camera angle. B) Clustered heatmap of autofluorescence from a dry (border) well. This visualization enables distinguishing pixels that cover the growth area, the border area of the well, and pixels that are located outside the well. C) Ranked pixel intensities, based on which the growth area of the cell culture within the ROI is defined (active pixels). D-E) Standard plate reader data output based on averaged fluorescence intensity for each well. Example traces (D) of co-cultures with 90'000 GLUT iN and 10'000 pA in the absence (left) and presence (right) of 30'000 GABA iN. E) Mean network spike frequency (left) and mean network spike amplitudes (right). F-G) Analyses of local field activity shown for each pixel. Visualization of well-averaged data in Figure 4 C by mean pixel average (F, left: mean spike frequency, middle: FWHM, right: mean spike amplitude, N = 2000 pixels, combined from 5 wells), or (G) separately for IN and OUT spikes (G, top: mean spike amplitude, bottom: FWHM). H) Pixel traces for the first 30 seconds of baseline calcium recording to illustrate GCaMP6f signal versus high-intensity autofluorescence signal from dry wells. I) Number of detected spikes in dependence of detection threshold applied. N = 5 wells (400 pixel/ well). Comparison of signals from culture is against the high autofluorescence intensity of dry wells. Box plots denote 2nd and 3rd quartile (gray), with bars extending to 1.5 times of the IQR. Individual datapoints are overlaid as dots. Line plots show the 95% confidence interval around the mean as semitransparent area. *$p<0.05$, .**$p<0.01$, ***$p<0.001$, n.s. = not significant.

Figure S6. GABA A receptor inhibition reverts effects of GABA iN on GLUT iN activity. (A-B) Standard plate reader data output based on well-averaged fluorescence intensity. A) Example trace showing activity of a d31 co-culture of 90'000 GLUT iN, 10'000 pA, with 30'000 GABA iN from one well at baseline over 5 minutes followed by 5 minutes in the presence of 5uM GABA A receptor antagonist bicuculline. B) Network spike frequency (left) and mean network spike amplitudes (right). (C-D) Analyses of local field activity shown for each pixel. Visualization of well-averaged data in Figure 5 B and C by pixel average (C, left: spike frequency, middle: FWHM, right: mean spike

amplitude, N = 2000 pixels, combined from 5 wells), or (D) separately for IN and OUT spikes (D, left: mean spike amplitude, right: FWHM). (E-G) Treatment of cultures with vehicle control (0.2% DMSO). E) Mean spike amplitude (left) and FWHM (right) of spikes in dependence of network spike participation. F) Spike detection in dependence of threshold and shown as fraction of total defined at a low prominence threshold of 0.1 (close to noise, as defined in Fig S5H-I), for IN spikes (left) and OUT spikes (right). G) (Pair-wise correlation of pixel intensities over time in dependence of distance between pixels, at baseline and in presence of DMSO. H) GABA concentration in the presence and absence of GABA iN. Dashed line denotes the detection limit of the assay. N = 5 wells per condition, Box plots denote 2nd and 3rd quartile (gray), with bars extending to 1.5 times of the IQR. Individual datapoints are overlaid as dots. Line plots show the 95% confidence interval around the mean, either as semitransparent area or error bars. *p<0.05, .**p<0.01, ***p<0.001, n.s. = not significant.

10 References

Baer, A., & Bode, J. (2001). Coping with kinetic and thermodynamic barriers: RMCE, an efficient strategy for the targeted integration of transgenes. *Current Opinion in Biotechnology*, *12*(5), 473–480. https://doi.org/10.1016/S0958-1669(00)00248-2

Bassil, R., Shields, K., Granger, K., Zein, I., Ng, S., & Chih, B. (2021). Improved modeling of human AD with an automated culturing platform for iPSC neurons, astrocytes and microglia. *Nature Communications*, *12*(1), Article 1. https://doi.org/10.1038/s41467-021-25344-6

Bertero, A., Pawlowski, M., Ortmann, D., Snijders, K., Yiangou, L., Cardoso de Brito, M., Brown, S., Bernard, W. G., Cooper, J. D., Giacomelli, E., Gambardella, L., Hannan, N. R. F., Iyer, D., Sampaziotis, F., Serrano, F., Zonneveld, M. C. F., Sinha, S., Kotter, M., & Vallier, L. (2016). Optimized inducible shRNA and CRISPR/Cas9 platforms for in vitro studies of human development using hPSCs. *Development*, *143*(23), 4405–4418. https://doi.org/10.1242/dev.138081

Brennand, K. J., Simone, A., Jou, J., Gelboin-Burkhart, C., Tran, N., Sangar, S., Li, Y., Mu, Y., Chen, G., Yu, D., McCarthy, S., Sebat, J., & Gage, F. H. (2011). Modelling schizophrenia using human induced pluripotent stem cells. *Nature*, *473*(7346), 221–225. https://doi.org/10.1038/nature09915

Canals, I., Ginisty, A., Quist, E., Timmerman, R., Fritze, J., Miskinyte, G., Monni, E., Hansen, M. G., Hidalgo, I., Bryder, D., Bengzon, J., & Ahlenius, H. (2018). Rapid and efficient induction of functional astrocytes from human pluripotent stem cells. *Nature Methods*, *15*(9), 693–696. https://doi.org/10.1038/s41592-018-0103-2

Chen, T.-W., Wardill, T. J., Sun, Y., Pulver, S. R., Renninger, S. L., Baohan, A., Schreiter, E. R., Kerr, R. A., Orger, M. B., Jayaraman, V., Looger, L. L., Svoboda, K., & Kim, D. S. (2013). Ultrasensitive fluorescent proteins for imaging neuronal activity. *Nature*, *499*(7458), 295–300. https://doi.org/10.1038/nature12354

Essayan-Perez, S., & Südhof, T. C. (2023). Neuronal γ-secretase regulates lipid metabolism, linking cholesterol to synaptic dysfunction in Alzheimer's disease. *Neuron*, *111*(20), 3176-3194.e7. https://doi.org/10.1016/j.neuron.2023.07.005

Hitoshi, N., Ken-ichi, Y., & Jun-ichi, M. (1991). Efficient selection for high-expression transfectants with a novel eukaryotic vector. *Gene*, *108*(2), 193–199. https://doi.org/10.1016/0378-1119(91)90434-D

Kolb, A. F. (2001). Selection-Marker-Free Modification of the Murine β-Casein Gene Using a *lox2722* Site. *Analytical Biochemistry*, *290*(2), 260–271. https://doi.org/10.1006/abio.2000.4984

Lin, J. (1991). Divergence measures based on the Shannon entropy. *IEEE Transactions on Information Theory*, *37*(1), 145–151. https://doi.org/10.1109/18.61115

Maaten, L. van der, & Hinton, G. (2008). Visualizing Data using t-SNE. *Journal of Machine Learning Research*, *9*(86), 2579–2605.

Meijer, M., Rehbach, K., Brunner, J. W., Classen, J. A., Lammertse, H. C. A., van Linge, L. A., Schut, D., Krutenko, T., Hebisch, M., Cornelisse, L. N., Sullivan, P. F., Peitz, M., Toonen, R.

F., Brüstle, O., & Verhage, M. (2019). A Single-Cell Model for Synaptic Transmission and Plasticity in Human iPSC-Derived Neurons. *Cell Reports*, *27*(7), 2199-2211.e6. https://doi.org/10.1016/j.celrep.2019.04.058

Melsted, P., Booeshaghi, A. S., Liu, L., Gao, F., Lu, L., Min, K. H. (Joseph), da Veiga Beltrame, E., Hjörleifsson, K. E., Gehring, J., & Pachter, L. (2021). Modular, efficient and constant-memory single-cell RNA-seq preprocessing. *Nature Biotechnology*, *39*(7), 813–818. https://doi.org/10.1038/s41587-021-00870-2

Mossink, B., van Rhijn, J.-R., Wang, S., Linda, K., Vitale, M. R., Zöller, J. E. M., van Hugte, E. J. H., Bak, J., Verboven, A. H. A., Selten, M., Negwer, M., Latour, B. L., van der Werf, I., Keller, J. M., Klein Gunnewiek, T. M., Schoenmaker, C., Oudakker, A., Anania, A., Jansen, S., … Nadif Kasri, N. (2022). Cadherin-13 is a critical regulator of GABAergic modulation in human stem-cell-derived neuronal networks. *Molecular Psychiatry*, *27*(1), 1–18. https://doi.org/10.1038/s41380-021-01117-x

O'Gorman, S., Fox, D. T., & Wahl, G. M. (1991). Recombinase-Mediated Gene Activation and Site-Specific Integration in Mammalian Cells. *Science*, *251*(4999), 1351–1355. https://doi.org/10.1126/science.1900642

Paşca, S. P., Portmann, T., Voineagu, I., Yazawa, M., Shcheglovitov, A., Paşca, A. M., Cord, B., Palmer, T. D., Chikahisa, S., Nishino, S., Bernstein, J. A., Hallmayer, J., Geschwind, D. H., & Dolmetsch, R. E. (2011). Using iPSC-derived neurons to uncover cellular phenotypes associated with Timothy syndrome. *Nature Medicine*, *17*(12), 1657–1662. https://doi.org/10.1038/nm.2576

Patzke, C., Han, Y., Covy, J., Yi, F., Maxeiner, S., Wernig, M., & Südhof, T. C. (2015). Analysis of conditional heterozygous STXBP1 mutations in human neurons. *The Journal of Clinical Investigation*, *125*(9), 3560–3571. https://doi.org/10.1172/JCI78612

Rhee, H. J., Shaib, A. H., Rehbach, K., Lee, C., Seif, P., Thomas, C., Gideons, E., Guenther, A., Krutenko, T., Hebisch, M., Peitz, M., Brose, N., Brüstle, O., & Rhee, J. S. (2019). An Autaptic Culture System for Standardized Analyses of iPSC-Derived Human Neurons. *Cell Reports*, *27*(7), 2212-2228.e7. https://doi.org/10.1016/j.celrep.2019.04.059

Saavedra, L., Wallace, K., Freudenrich, T. F., Mall, M., Mundy, W. R., Davila, J., Shafer, T. J., Wernig, M., & Haag, D. (2021). Comparison of Acute Effects of Neurotoxic Compounds on Network Activity in Human and Rodent Neural Cultures. *Toxicological Sciences: An Official Journal of the Society of Toxicology*, *180*(2), 295–312. https://doi.org/10.1093/toxsci/kfab008

Schmid, B., Holst, B., Poulsen, U., Jørring, I., Clausen, C., Rasmussen, M., Mau-Holzmann, U. A., Steeg, R., Nuthall, H., Ebneth, A., & Cabrera-Socorro, A. (2021). Generation of two gene edited iPSC-lines carrying a DOX-inducible NGN2 expression cassette with and without GFP in the AAVS1 locus. *Stem Cell Research*, *52*, 102240. https://doi.org/10.1016/j.scr.2021.102240

Schmidt, U., Weigert, M., Broaddus, C., & Myers, G. (2018). Cell Detection with Star-Convex Polygons. *Medical Image Computing and Computer Assisted Intervention – MICCAI 2018: 21st International Conference, Granada, Spain, September 16-20, 2018, Proceedings, Part II*, 265–273. https://doi.org/10.1007/978-3-030-00934-2_30

Shan, X., Zhang, A., Rezzonico, M. G., Tsai, M.-C., Sanchez-Priego, C., Zhang, Y., Chen, M. B., Choi, M., Andrade López, J. M., Phu, L., Cramer, A. L., Zhang, Q., Pattison, J. M., Rose, C. M., Hoogenraad, C. C., & Jeong, C. G. (2024). Fully defined NGN2 neuron protocol reveals

diverse signatures of neuronal maturation. *Cell Reports Methods*, 100858. https://doi.org/10.1016/j.crmeth.2024.100858

Shcheglovitov, A., Shcheglovitova, O., Yazawa, M., Portmann, T., Shu, R., Sebastiano, V., Krawisz, A., Froehlich, W., Bernstein, J. A., Hallmayer, J. F., & Dolmetsch, R. E. (2013). SHANK3 and IGF1 restore synaptic deficits in neurons from 22q13 deletion syndrome patients. *Nature*, *503*(7475), 267–271. https://doi.org/10.1038/nature12618

Shih, P.-Y., Kreir, M., Kumar, D., Seibt, F., Pestana, F., Schmid, B., Holst, B., Clausen, C., Steeg, R., Fischer, B., Pita-Almenar, J., Ebneth, A., & Cabrera-Socorro, A. (2021). Development of a fully human assay combining NGN2-inducible neurons co-cultured with iPSC-derived astrocytes amenable for electrophysiological studies. *Stem Cell Research*, *54*, 102386. https://doi.org/10.1016/j.scr.2021.102386

Song, S., Ashok, A., Williams, D., Kaufman, M., Duff, K., & Sproul, A. (2021). Efficient derivation of excitatory and inhibitory neurons from human pluripotent stem cells stably expressing direct reprogramming factors. *Current Protocols*, *1*(6), e141. https://doi.org/10.1002/cpz1.141

Sun, Z., & Südhof, T. C. (2021). A simple Ca2+-imaging approach to neural network analyses in cultured neurons. *Journal of Neuroscience Methods*, *349*, 109041. https://doi.org/10.1016/j.jneumeth.2020.109041

Takahashi, K., Tanabe, K., Ohnuki, M., Narita, M., Ichisaka, T., Tomoda, K., & Yamanaka, S. (2007). Induction of Pluripotent Stem Cells from Adult Human Fibroblasts by Defined Factors. *Cell*, *131*(5), 861–872. https://doi.org/10.1016/j.cell.2007.11.019

Virtanen, P., Gommers, R., Oliphant, T. E., Haberland, M., Reddy, T., Cournapeau, D., Burovski, E., Peterson, P., Weckesser, W., Bright, J., Van Der Walt, S. J., Brett, M., Wilson, J., Millman, K. J., Mayorov, N., Nelson, A. R. J., Jones, E., Kern, R., Larson, E., … Vázquez-Baeza, Y.

(2020). SciPy 1.0: Fundamental algorithms for scientific computing in Python. *Nature Methods*, *17*(3), 261–272. https://doi.org/10.1038/s41592-019-0686-2

Weigert, M., & Schmidt, U. (2022). Nuclei Instance Segmentation and Classification in Histopathology Images with Stardist. *2022 IEEE International Symposium on Biomedical Imaging Challenges (ISBIC)*, 1–4. https://doi.org/10.1109/ISBIC56247.2022.9854534

Wolf, F. A., Angerer, P., & Theis, F. J. (2018). SCANPY: Large-scale single-cell gene expression data analysis. *Genome Biology*, *19*(1), 15. https://doi.org/10.1186/s13059-017-1382-0

Xing, W., de Lima, A. D., & Voigt, T. (2021). The Structural E/I Balance Constrains the Early Development of Cortical Network Activity. *Frontiers in Cellular Neuroscience*, *15*. https://doi.org/10.3389/fncel.2021.687306

Yang, N., Chanda, S., Marro, S., Ng, Y.-H., Janas, J. A., Haag, D., Ang, C. E., Tang, Y., Flores, Q., Mall, M., Wapinski, O., Li, M., Ahlenius, H., Rubenstein, J. L., Chang, H. Y., Buylla, A. A., Südhof, T. C., & Wernig, M. (2017). Generation of pure GABAergic neurons by transcription factor programming. *Nature Methods*, *14*(6), 621–628. https://doi.org/10.1038/nmeth.4291

Zhang, Y., Pak, C., Han, Y., Ahlenius, H., Zhang, Z., Chanda, S., Marro, S., Patzke, C., Acuna, C., Covy, J., Xu, W., Yang, N., Danko, T., Chen, L., Wernig, M., & Südhof, T. C. (2013). Rapid Single-Step Induction of Functional Neurons from Human Pluripotent Stem Cells. *Neuron*, *78*(5), 785–798. https://doi.org/10.1016/j.neuron.2013.05.029

Zushin, P.-J. H., Mukherjee, S., & Wu, J. C. (2023). FDA Modernization Act 2.0: Transitioning beyond animal models with human cells, organoids, and AI/ML-based approaches. *The Journal of Clinical Investigation*, *133*(21). https://doi.org/10.1172/JCI175824

Fig 1

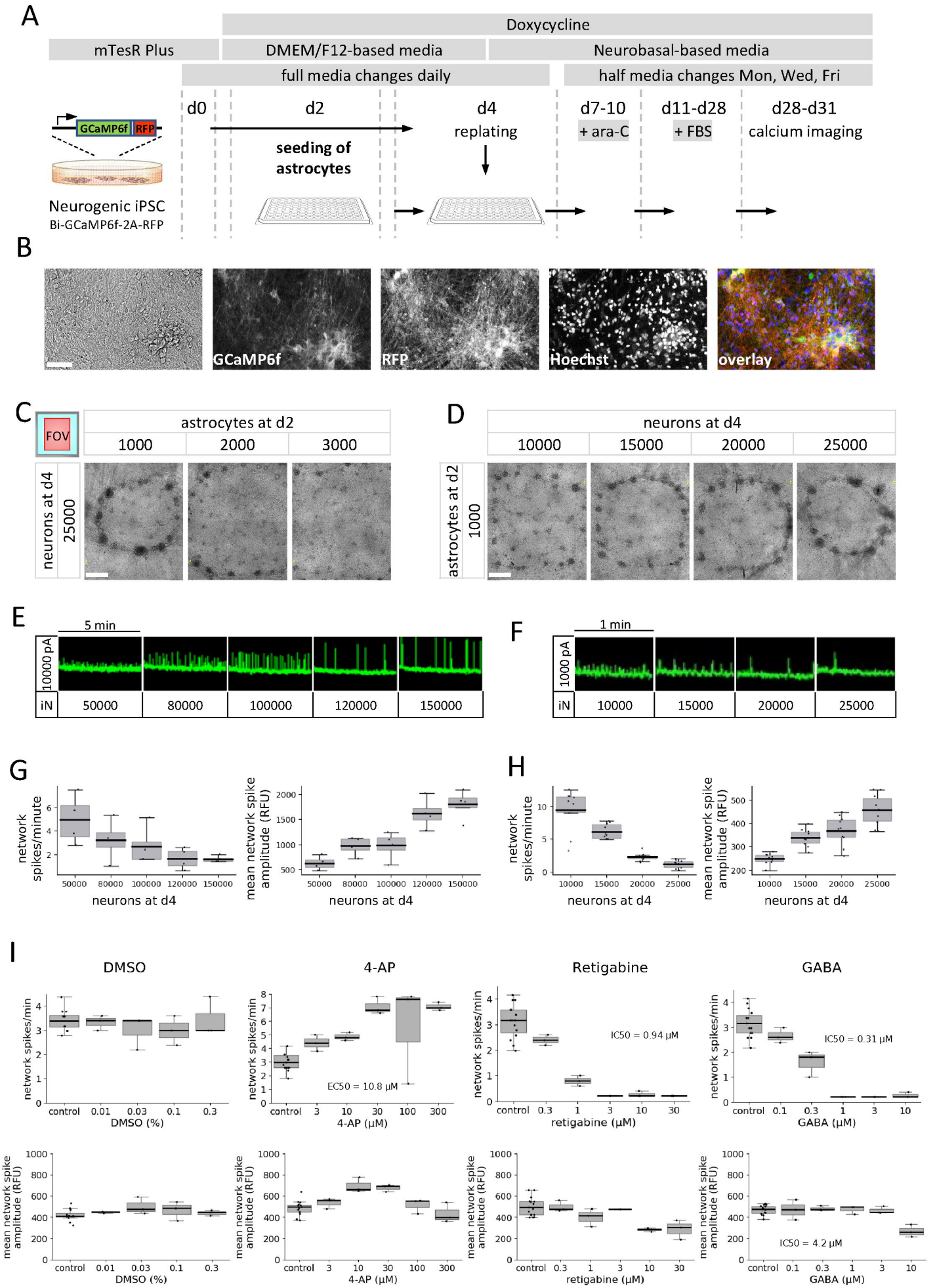
A
Doxycycline
mTesR Plus
DMEM/F12-based media
Neurobasal-based media
full media changes daily
half media changes Mon, Wed, Fri
GCaMP6f
RFP
Neurogenic iPSC
Bi-GCaMP6f-2A-RFP
d0
d2
seeding of astrocytes
d4
replating
d7-10
+ ara-C
d11-d28
+ FBS
d28-d31
calcium imaging
B
GCaMP6f
RFP
Hoechst
overlay
C
FOV
astrocytes at d2
1000
2000
3000
neurons at d4
25000
D
neurons at d4
10000
15000
20000
25000
astrocytes at d2
1000
E
5 min
10000 pA
iN
50000
80000
100000
120000
150000
F
1 min
1000 pA
iN
10000
15000
20000
25000
G
network spikes/minute
mean network spike amplitude (RFU)
neurons at d4
H
network spikes/minute
mean network spike amplitude (RFU)
neurons at d4
I
DMSO
4-AP
Retigabine
GABA
network spikes/min
mean network spike amplitude (RFU)
DMSO (%)
4-AP (µM)
retigabine (µM)
GABA (µM)
EC50 = 10.8 µM
IC50 = 0.94 µM
IC50 = 0.31 µM
IC50 = 4.2 µM

Fig 2

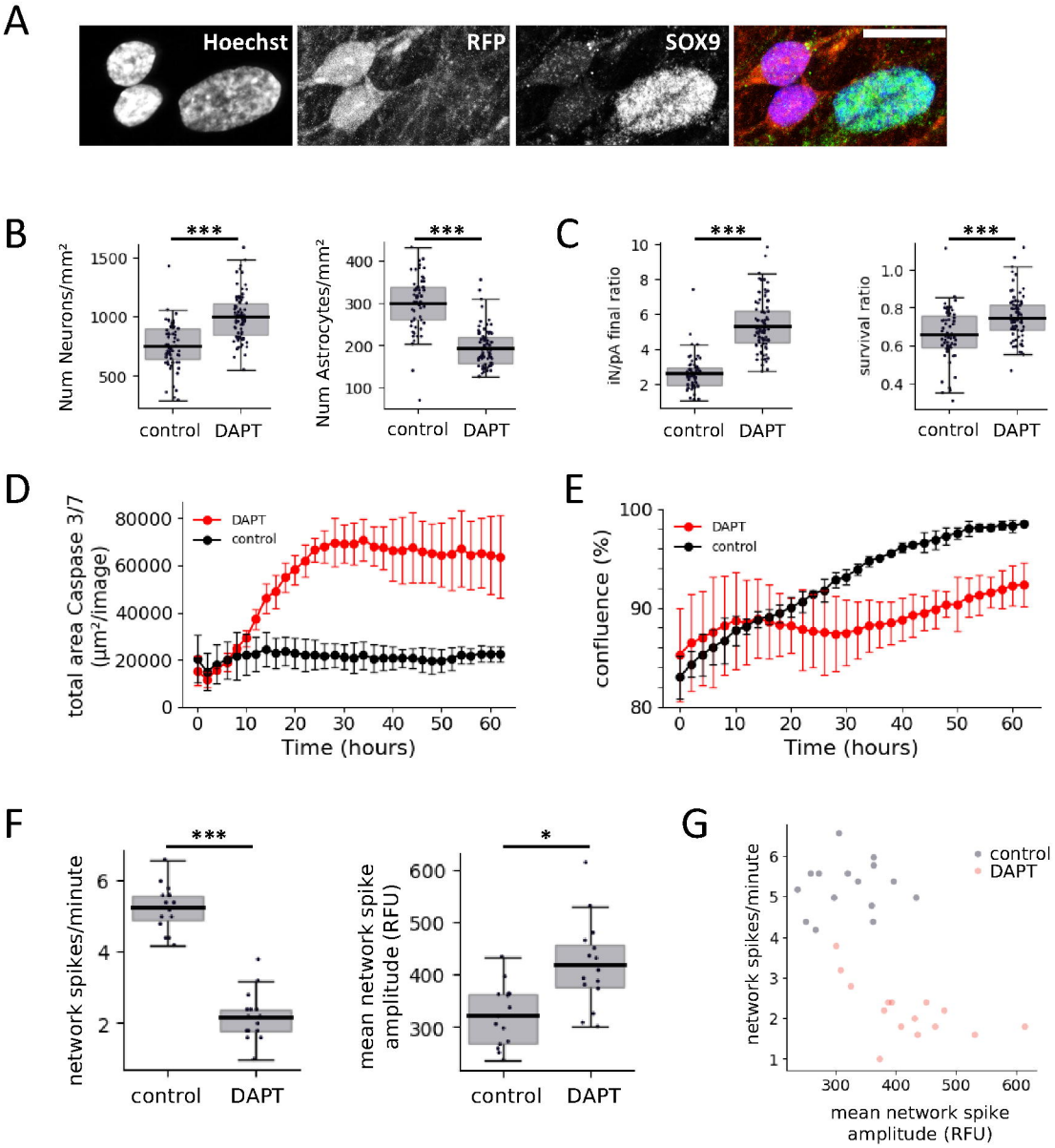
A
Hoechst
RFP
SOX9
B
Num Neurons/mm²
Num Astrocytes/mm²
control
DAPT
***
C
iN/pA final ratio
survival ratio
D
total area Caspase 3/7 (µm²/image)
Time (hours)
E
confluence (%)
F
network spikes/minute
mean network spike amplitude (RFU)
*
G
mean network spike amplitude (RFU)

Fig 3

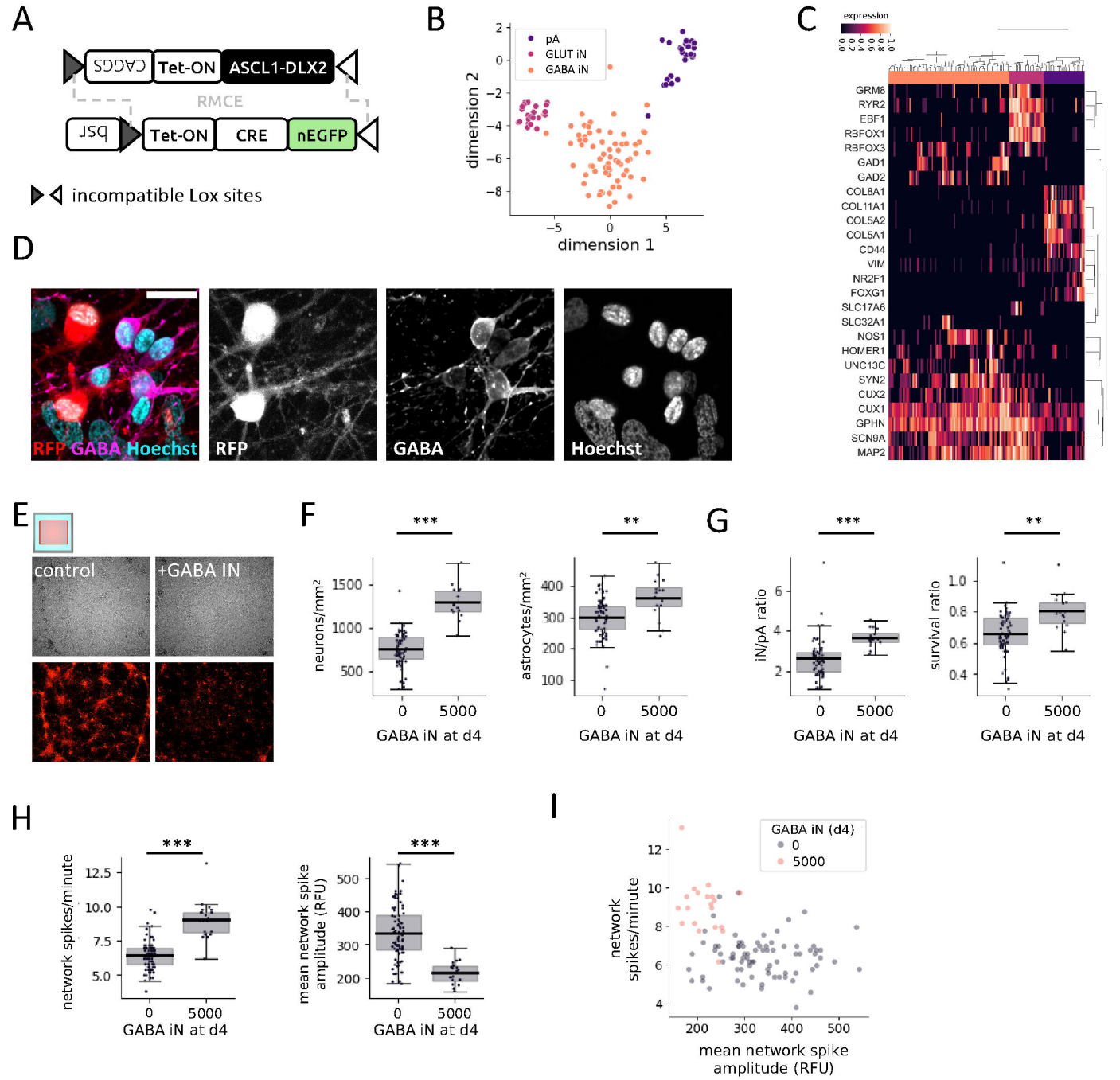
A
CAGGS
Tet-ON
ASCL1-DLX2
RMCE
bsr
Tet-ON
CRE
nEGFP
incompatible Lox sites
B
pA
GLUT iN
GABA iN
dimension 2
dimension 1
C
expression
GRM8
RYR2
EBF1
RBFOX1
RBFOX3
GAD1
GAD2
COL8A1
COL11A1
COL5A2
COL5A1
CD44
VIM
NR2F1
FOXG1
SLC17A6
SLC32A1
NOS1
HOMER1
UNC13C
SYN2
CUX2
CUX1
GPHN
SCN9A
MAP2
D
RFP GABA Hoechst
RFP
GABA
Hoechst
E
control
+GABA IN
F
neurons/mm²
astrocytes/mm²
GABA iN at d4
G
iN/pA ratio
survival ratio
GABA iN at d4
H
network spikes/minute
mean network spike amplitude (RFU)
GABA iN at d4
I
GABA iN (d4)
0
5000
network spikes/minute
mean network spike amplitude (RFU)

Fig 4

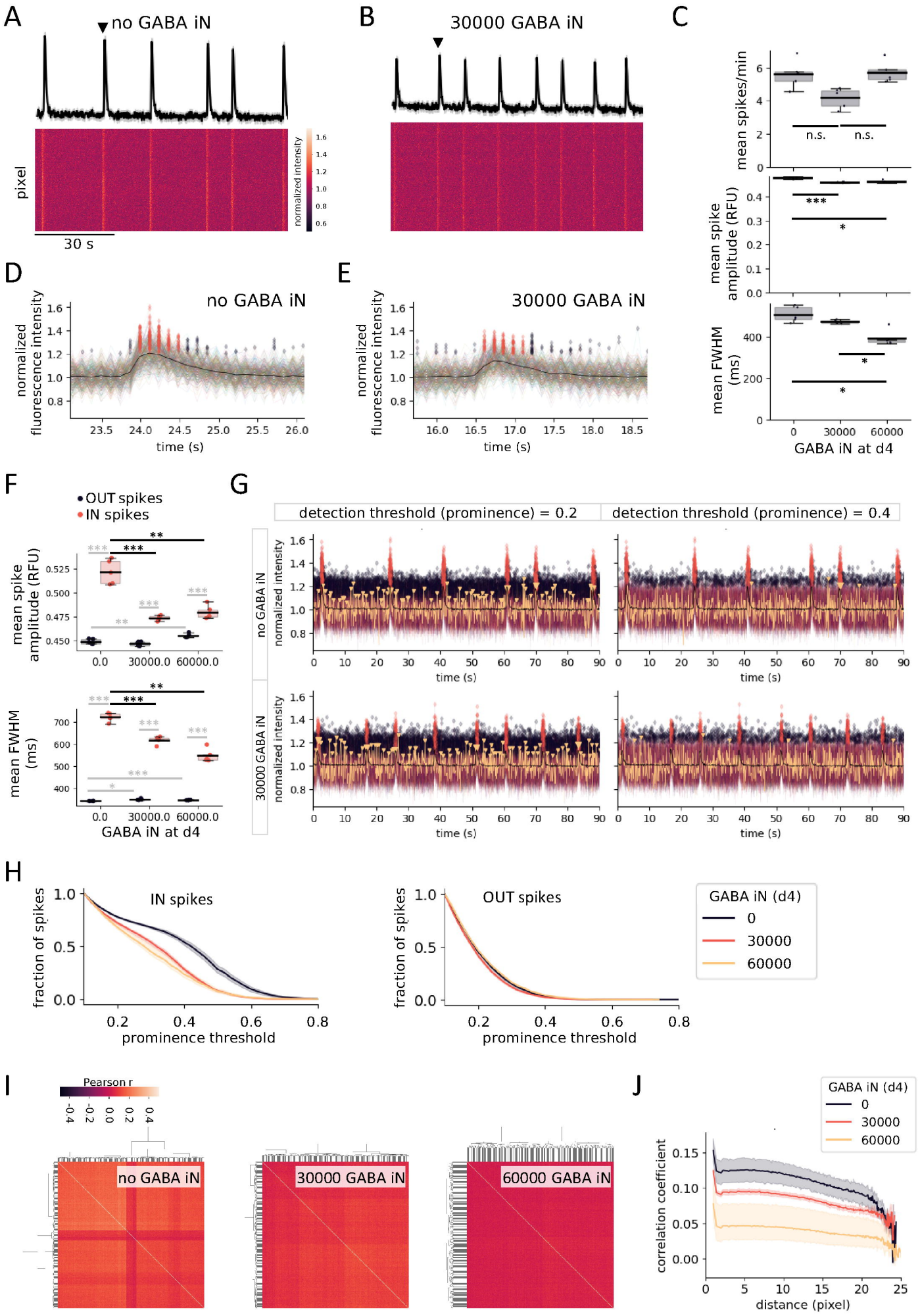
A
no GABA iN
pixel
30 s
normalized intensity
B
30000 GABA iN
C
mean spikes/min
n.s.
n.s.
mean spike amplitude (RFU)
***
*
mean FWHM (ms)
*
*
0
30000
60000
GABA iN at d4
D
no GABA iN
normalized fluorescence intensity
time (s)
E
30000 GABA iN
normalized fluorescence intensity
time (s)
F
OUT spikes
IN spikes
mean spike amplitude (RFU)
mean FWHM (ms)
GABA iN at d4
G
detection threshold (prominence) = 0.2
detection threshold (prominence) = 0.4
no GABA iN
30000 GABA iN
normalized intensity
time (s)
H
IN spikes
OUT spikes
fraction of spikes
prominence threshold
GABA iN (d4)
0
30000
60000
I
Pearson r
no GABA iN
30000 GABA iN
60000 GABA iN
J
GABA iN (d4)
0
30000
60000
correlation coefficient
distance (pixel)

Fig 5

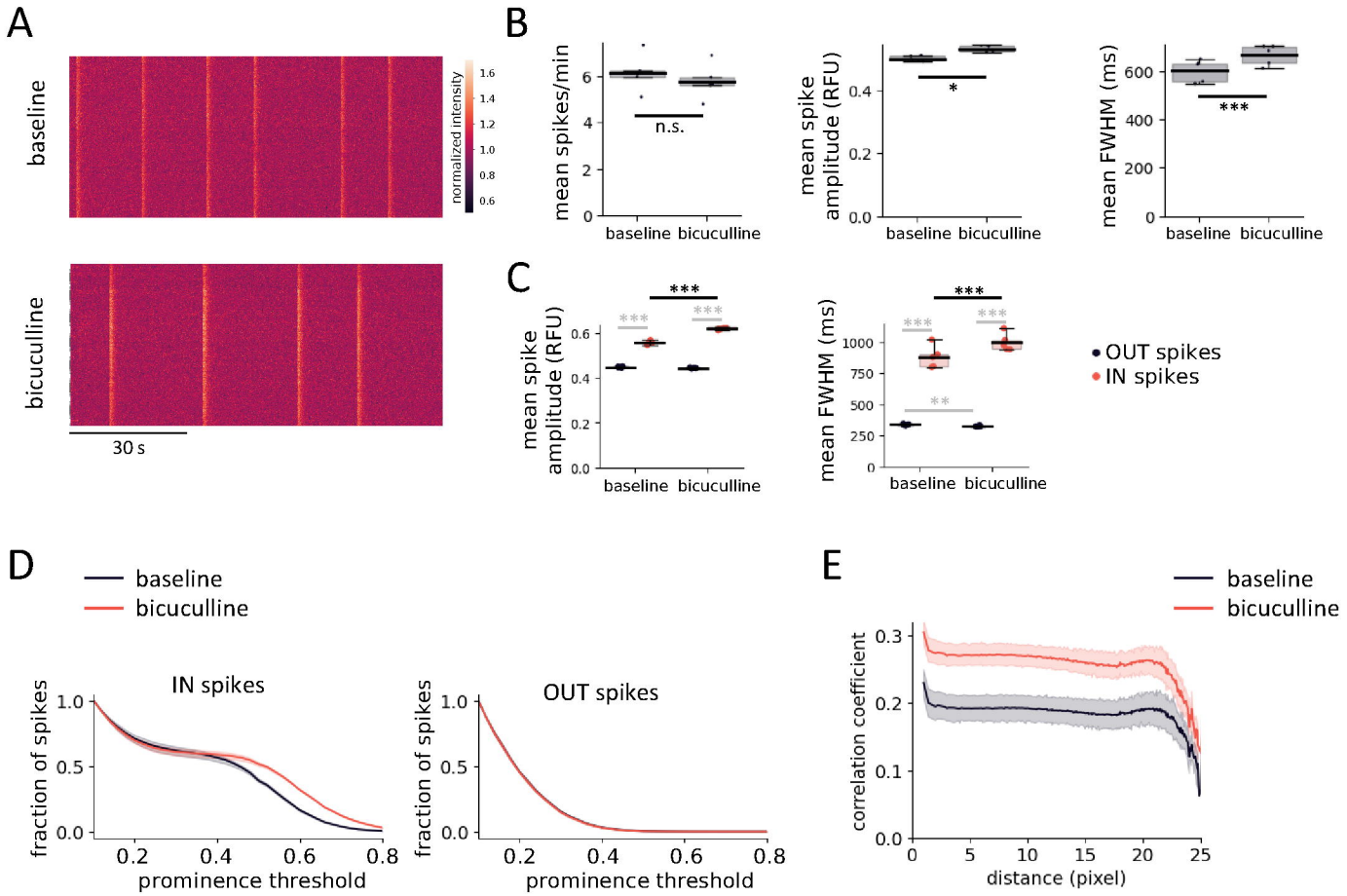
A
baseline
bicuculline
normalized intensity
1.6
1.4
1.2
1.0
0.8
0.6
30 s
B
mean spikes/min
n.s.
mean spike amplitude (RFU)
*
mean FWHM (ms)
***
baseline
bicuculline
C
mean spike amplitude (RFU)
mean FWHM (ms)
***
**
OUT spikes
IN spikes
D
baseline
bicuculline
IN spikes
OUT spikes
fraction of spikes
prominence threshold
E
correlation coefficient
distance (pixel)